Analysing the limitations of the dual-porosity response during well tests in naturally fractured reservoirs

Egya, D. O.; Geiger, S.; Corbett, P. W.M.; March, R.; Bisdom, K.; Bertotti, G.; Bezerra, F. H.

DOI
10.1144/petgeo2017-053

Publication date
2019

Document Version
Final published version

Published in
Petroleum Geoscience

PG
Petroleum Geoscience

Research article

Published online January 17, 2018 https://doi.org/10.1144/petgeo2017-053 | Vol. 25 | 2019 | pp. 30–49

Analysing the limitations of the dual-porosity response during well tests in naturally fractured reservoirs

D. O. Egya[1*], S. Geiger[1], P. W. M. Corbett[1], R. March[1], K. Bisdom[2], G. Bertotti[2] & F. H. Bezerra[3]

[1] Institute of Petroleum Engineering, Heriot-Watt University, Edinburgh EH14 4AS, UK
[2] Department of Geoscience and Engineering, Delft University of Technology, Stevinweg 1, 2628CN Delft, The Netherlands
[3] Department of Geology, Federal University Rio Grande do Norte, Natal, Rio Grande do Norte, Brazil
D.O.E., 0000-0001-8974-3617; R.M., 0000-0001-6493-9138; K.B., 0000-0003-3619-2756
* Correspondence: doe1@hw.ac.uk

Abstract: Geological reservoirs can be extensively fractured but the well-test signatures observed in the wells may not show a pressure transient response that is representative of naturally fractured reservoirs (NFRs): for example, one that indicates two distinct pore systems (i.e. the mobile fractures and immobile matrix). Yet, the production behaviour may still be influenced by these fractures. To improve the exploitation of hydrocarbons from NFRs, we therefore need to improve our understanding of fluid-flow behaviour in fractures.

Multiple techniques are used to detect the presence and extent of fractures in a reservoir. Of particular interest to this work is the analysis of well-test data in order to interpret the flow behaviour in an NFR. An important concept for interpreting well-test data from an NFR is the theory of dual-porosity model. However, several studies pointed out that the dual-porosity model may not be appropriate for interpreting well tests from all fractured reservoirs.

This paper therefore uses geological well-testing insights to explore the limitations of the characteristic flow behaviour inherent to the dual-porosity model in interpreting well-test data from Type II and III NFRs of Nelson's classification. To achieve this, we apply a geoengineering workflow with discrete fracture matrix (DFM) modelling techniques and unstructured-grid reservoir simulations to generate synthetic pressure transient data in both idealized fracture geometries and real fracture networks mapped in an outcrop of the Jandaira Formation. We also present key reservoir features that account for the classic V-shape pressure derivative response in NFRs. These include effects of fracture skin, a very tight matrix permeability and wells intersecting a minor, unconnected fracture close to a large fracture or fracture network. Our findings apply to both connected and disconnected fracture networks.

Received 26 April 2017; **revised** 30 November 2017; **accepted** 4 December 2017

Many sedimentary formations, as well as basement reservoirs, contain naturally occurring fractures, and, hence, naturally fractured reservoirs (NFRs) account for a significant amount of the remaining conventional hydrocarbon across the globe (Bourbiaux 2010; Lemonnier & Bourbiaux 2010*b*; Spence *et al.* 2014). Many operating companies now follow the advice that 'all reservoirs should be considered fractured until proven otherwise' (Narr *et al.* 2006). This approach is driven by the fact that fractures often have an adverse impact on hydrocarbon production, leading to early water breakthrough, irregular drainage and sweep patterns, and low recovery factors, as often much of the hydrocarbons are left behind in the less permeable rock matrix (Gilman & Kazemi 1983; Firoozabadi 2000). To improve the exploitation of hydrocarbons from this type of reservoir, we need to improve our understanding of the nature and behaviour of the fractures, and the degree to which they influence reservoir performance early during the field development. This knowledge enables us to develop suitable field-development strategies for NFRs, such as the positioning of wells, planning of water flooding and improved oil recovery (IOR)/enhanced oil recovery (EOR) methods (e.g. Beliveau *et al.* 1993; Wei *et al.* 1998; Nelson 2001; Fernø 2012).

Multiple geological, petrophysical and geophysical techniques, including the use of outcrop analogues, seismic attributes, log data (including image logs), production data, geomechanical simulations and reservoir simulations, are typically integrated to: first, detect the presence and extent of fractures in a reservoir; secondly, to characterize and model the fractures; and, lastly, to understand whether the fractures enhance production or provide barriers to fluid flow (Spence *et al.* 2014).

Pressure transient data obtained during well testing can offer important information as to whether a reservoir is fractured or not and can identify flow behaviours, especially during the appraisal and development stage (e.g. Earlougher 1977; Bourdet 2002). An important concept for identifying and analysing NFRs from well-test data is the theory of the dual-porosity model (also sometimes referred to as the double-porosity model: e.g. Warren & Root 1963; Gringarten 1984, 1987; Moench 1984; Chen 1989). This model was first proposed by Barenblatt *et al.* (1960) to simulate flow behaviour in fractured reservoirs, and developed by Warren & Root (1963) to model pressure transient behaviour in well test from NFRs. It has been the industry standard for modelling NFRs and interpreting well-test data from NFRs for more than 50 years (Chen 1989; Cinco-Ley 1996; Bourdet 2002; Syihab 2009; Lemonnier & Bourbiaux 2010*a*; Kuchuk & Biryukov 2014; Morton *et al.* 2015). The dual-porosity model consists of two regions with distinct porosities and permeability, representing the matrix and fractures within the formation (Fig. 1a and b). The matrix constitutes the region with negligible flow capacity but significant pore volume that is providing the primary porosity to the reservoir system. The fracture system provides the main path and capacity for fluid flow from the formation to the well but has low porosity. The dual-porosity model only considers matrix-fracture and fracture-fracture flow but not matrix-matrix exchange. However, this model can be extended to a dual-permeability model, which assumes that the matrix is permeable and allows for flows between matrix blocks (Lemonnier & Bourbiaux 2010*a*, *b*).

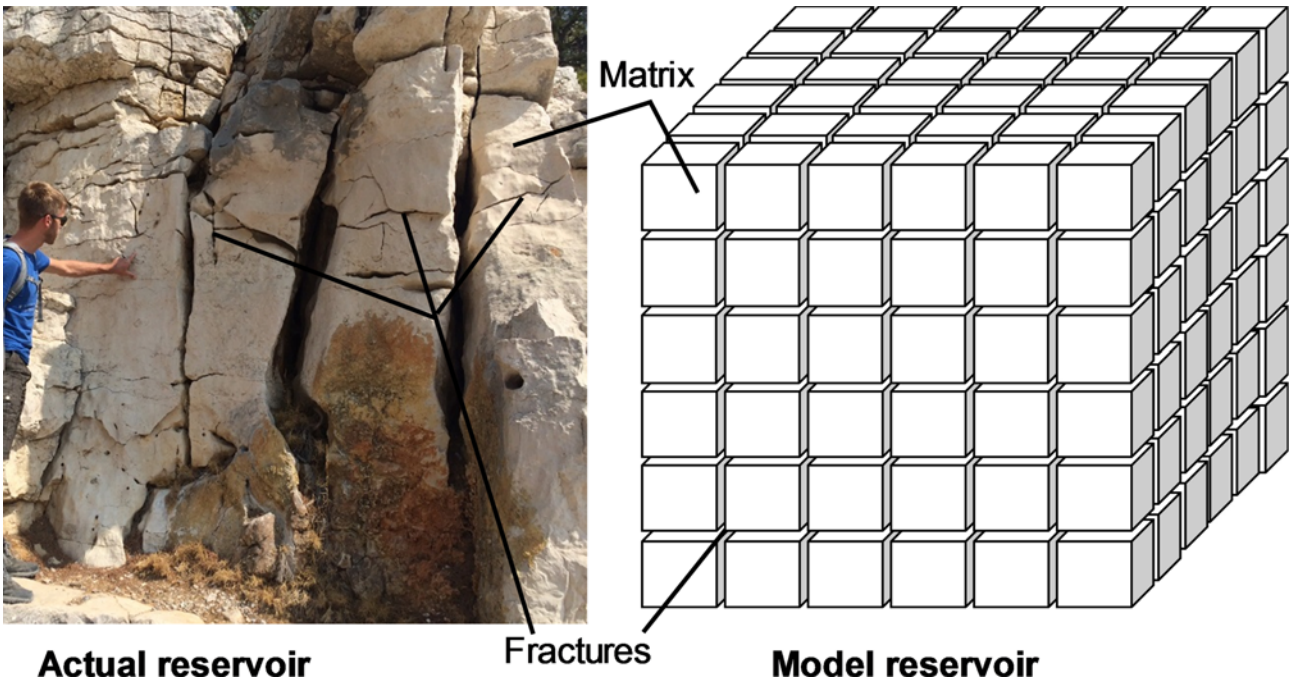

Fig. 1. Idealization of a dual-porosity medium. (**a**) Fractured and jointed carbonate reservoir image at the well-test scale from the Cap Câble analogue (Barremian, Lower Cretaceous, Cassis, France) used for many carbonate fields; and (**b**) simulation reservoir model. (Modified from Warren & Root 1963.)

Warren & Root (1963) introduced the first technique for identification and interpretation of NFRs. Their theoretical results, which were reproduced by Kazemi (1969) (see Fig. 2), show that the pressure drop or build-up on a semi-log plot is characterized by two parallel straight lines related to the two distinct regions (dual porosities) in the reservoir. The first straight line (A) indicates the pseudo-radial flow from the fracture system. This is followed by the transition period (B) when depleted fractures are recharged by the matrix discharge until both systems attain equilibrium. Pressure stabilization in the two systems yield the second straight line (radial flow) (C). The development of the pressure derivatives and type curves (Bourdet & Gringarten 1980; Bourdet *et al*. 1983*a*, *b*, 1989; Gringarten 1987) provide more efficient ways to diagnose dual-porosity behaviour, and to determine permeability thickness (*kh*) and fracture volumes in NFRs. They also aid the identification of other flow regimes that are not discernible by the semi-log plot (Fig. 2). On the log–log analysis plot (Fig. 3), the Warren & Root (1963) dual-porosity model is depicted by a dual-porosity 'dip' (V-shape) – a minimum on the pressure derivative profile (B) sandwiched between the first stabilization (corresponding to a period of flow from the fracture system, A) and the second stabilization (the combined flow from the both fracture and the matrix system, C).

Nelson (2001) classified NFRs into four categories, depending on the contribution of fractures to the reservoir quality and recovery:

- Type I: fractures provide the required reservoir porosity and permeability to produce a reservoir.
- Type II: fractures provide the essential reservoir permeability to produce a reservoir.
- Type III: fractures contribute permeability to an already producible reservoir.
- Type IV: fractures contribute no additional porosity or permeability but create significant barriers to a reservoir flow.

Based on the above categories, the assumptions inherent in the Warren & Root (1963) dual-porosity model are only applicable to Type II of Nelson's (2001) classification where the matrix is stagnant but not all dual-porosity (fracture–matrix) systems.

Several studies, including Wei *et al.* (1998), Corbett *et al.* (2012), Morton *et al.* (2012, 2013), Agada *et al.* (2014), Kuchuk & Biryukov (2014, 2015), Morton *et al.* (2015) and Egya *et al.* (2016, 2017) have demonstrated that the pressure behaviour in an NFR can be notably different from the theoretical dual-porosity behaviour predicted for a heavily fractured NFR with well-connected fracture networks. In these cases, the pressure responses do not exhibit the classical dual-porosity behaviour, and, hence, the use of the Warren & Root (1963) dual-porosity model may not be appropriate for identification and interpretation of all NFRs, particularly for moderately and/or discretely fractured reservoirs. This raises the important question of what properties of the fracture network cause the dual-porosity signal to be absent in some NFRs and to be present in others. Since the location, orientation and connectivity of fractures are very difficult to quantify directly and unambigously in the reservoir, linking known properties of the fracture network to the dynamic response during a well test remains elusive.

Traditionally, outcrop analogue data have been used for fracture characterization as they allow for a more direct and detailed observation of the key geological features and principal reservoir properties that could control reservoir performance (Seers & Hodgetts 2013; Geiger & Matthäi 2014; Howell *et al.* 2014). This characterization typically focuses on the static properties, and may be difficult to be scaled and linked to possible subsurface dynamic behaviours. However, new simulation approaches that employ unstructured grids enable us to model mapped outcrop fracture patterns, together with petrophysical data that are representative of a given subsurface reservoir. This way, a numerical simulation model allows us to understand how fractures impact flow behaviours and how this behaviour could be upscaled (Wilson *et al.* 2011; Geiger & Matthäi 2014). The numerical approach is often termed the discrete fracture and matrix (DFM) method (e.g. Kim & Deo 2000; Bogdanov *et al.* 2003; Karimi-Fard *et al.* 2004), as it enables us to explicitly represent the structure and geometry of both fracture network and rock matrix in the flow simulations. Applications of the DFM approach that employed outcrop-based fracture patterns include, but are not limited to, single-phase upscaling of multiscale fracture networks (e.g. Matthäi & Belayneh 2004; Ahmadov *et al.* 2007; Zhou *et al.* 2014; Hardebol *et al.* 2015; Bisdom *et al.* 2016),

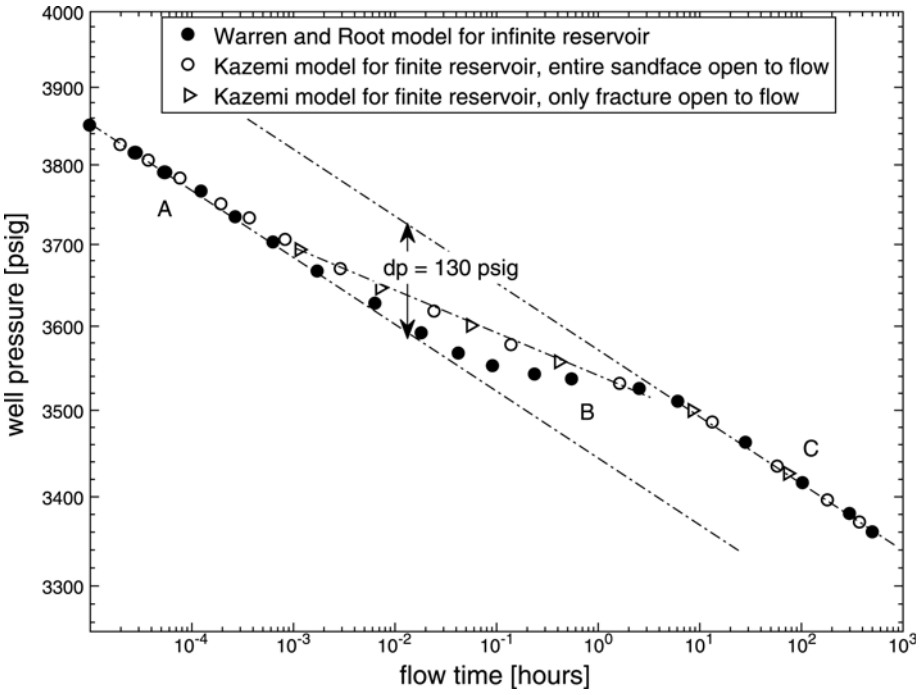

Fig. 2. Pressure drawdown according to the model by Warren & Root, and Kazemi (modified from Kazemi 1969). 'dp' denotes the vertical separation of the drawdown curve.

and simulating synthetic well-test signals in fractured formations (Matthäi & Roberts 1996; Corbett *et al.* 2012). Other applications are quantifying the characteristics of heat flow in geothermal systems (Geiger & Emmanuel 2010) and contaminant transport in fractured aquifers (Geiger & Emmanuel 2010; Edery *et al.* 2016), or analysing multiphase flow displacement processes in fractured sedimentary formations (e.g. Belayneh *et al.* 2006, 2007, 2009; Geiger *et al.* 2009, 2013; Agar *et al.* 2010).

In this study, we will use DFM and unstructured-grid reservoir-simulation technologies in combination with multiscale fracture patterns from outcrop data, and apply a geoengineering workflow (Corbett *et al.* 2012) to quantify how fracture-network characteristics, matrix properties and well locations impact the pressure transient behaviour observed in well tests. The results then allow us to quantify, in a rigorous and systematic way, when and why the assumptions inherent to the dual-porosity model break down when interpreting well-test data from NFRs. Firstly, we review the basic theory of well testing in NFRs. We then discuss the geoengineering workflow used in this study and describe the available field data. This is followed by a brief description on how our simulation models are generated and validated. Finally, we present simulation results and observations, and, finally, the conclusions. This paper deals with natural fractures with Type II and III properties of Nelson's (2001) classification. Modelling of hydraulic fractures and vugs are out of the scope of this study. Furthermore, uniform fracture conductivity (either finite or infinite) are assumed in all fracture configurations presented.

Theory of well testing in an NFR

The dual-porosity model of Warren & Root (1963) model assumes a continuum approach in which matrix and fracture systems are considered to be continuous and uniform throughout the reservoir. Two characteristic parameters control the deviation of the dual-porosity systems from the homogeneous reservoir. These parameters are the storativity ratio and the interporosity flow coefficient. The storativity ratio ω is defined as the ratio of fluid stored in fracture system to that of the total reservoir system:

$$\omega = \frac{\varphi_f C_f}{\varphi_f C_f + \varphi_m C_m} \tag{1}$$

where φ_f, φ_m, C_f and C_m denote fracture porosity, matrix porosity, fracture compressibility and matrix compressibility, respectively.

The interporosity flow coefficient, λ, reflects the contrast between the permeability of the matrix and fracture – that is, it is a measure of the ability of the fluid to flow from the matrix into the fractures:

$$\lambda = \alpha r_w^2 \frac{k_m}{k_f} \tag{2}$$

where r_w, k_m and k_f denote well radius, matrix permeability and

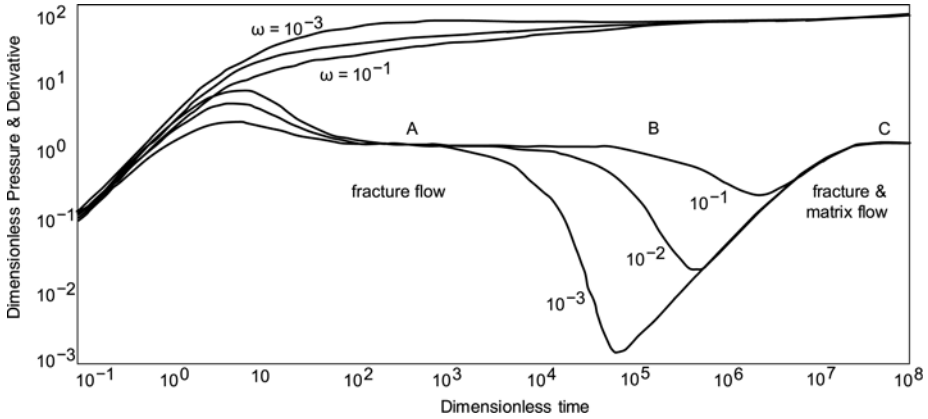

Fig. 3. Dual-porosity V-shape on a log–log plot showing the influence of the storativity ratio '(ω)' on the pressure derivative. Interporosity flow coefficient (λ) = 10^{-7}. (Modified from Bourdet 2002.)

fracture permeability, respectively; α is a shape factor that depends on the size and geometry of the matrix.

Warren & Root (1963) also assumed that the interporosity flow from matrix to fractures occurs under pseudo-steady state (PSS) conditions. PSS interporosity flow (PSSIF) supposes that, at any given time, the flow and pressure at all points in the matrix blocks is distributed equally, resulting in uniform transfer within the matrix and between the matrix and fracture. Other authors, including Odeh (1965), Kazemi *et al.* (1969), Streltsova (1976) and Mavor & Cinco-Ley (1979), subsequently shared this assumption. Kazemi (1969), de Swaan (1976), Boulton & Streltsova (1977), Najurieta (1980), Cinco-Ley & Samaniego (1982), Serra *et al.* (1983) and Streltsova (1983) all developed alternatives that overcome the PSSIF assumption and proposed transient interporosity flow (TIF) between fracture and matrix (i.e. the pressure in the matrix blocks can vary locally). This implies that, although the response to pressure changes for a fracture intersecting a well is faster in the fracture system compared to the matrix, both systems respond simultaneously at the early time of flow. The TIF assumption argues that PSSIF would be reached only after a considerable period of flow.

Warren & Root's (1963) original model did not consider the effect of wellbore storage and skin. Mavor & Cinco-Ley (1979) added the wellbore effects. Bourdet & Gringarten (1980) extended Mavor & Cinco-Ley's (1979) wellbore storage effect to the TIF model. Moench (1984) and Cinco-Ley *et al.* (1985) further showed that the early PSSIF regime can be linked to a skin effect (damage at the surface of the blocks) between the matrix and the fractures. Under these restricted interporosity flow conditions, the partial plugging of fractures caused by mineralization or any form of formation damage results in permeability reduction normal to the fracture face, thus allowing an impaired flow of fluid discharged from the matrix to the fractures. Both PSSIF and TIF flow conditions have been found in fields and/or presented in the literature (Gringarten 1984; Wei *et al.* 1998; Bourdet 2002; Kuchuk *et al.* 2015), leading to a debate as to which of these assumptions is more reliable and justified in modelling and interpreting NFRs. Recent studies suggest that neither form, PSSIF nor TIF, of the dual-porosity model assumptions may be adequate to interpret well-test data from certain NFRs (e.g. discrete fracture networks) (Wei *et al.* 1998; Corbett *et al.* 2012; Morton *et al.* 2012, 2013; Agada *et al.* 2014; Kuchuk & Biryukov 2014, 2015; Morton *et al.* 2015).

Methodology and data

Geoengineering workflow

In order to appropriately evaluate the flow behaviour of fractures on pressure transient data from NFRs, we adopted the geoengineering workflow of Corbett *et al.* (2012) (see Fig. 4). At the heart of the geoengineering workflow lies the numerical simulation of the diffusivity equation:

$$\phi C_t \frac{\partial p}{\partial t} = \nabla \left[\frac{\boldsymbol{k}(\boldsymbol{x})}{\mu} \nabla p \right] \tag{3}$$

for given reservoir properties and reservoir geometries, where p, t and C_t denote pressure, time and total compressibility, respectively. $\boldsymbol{k}(\boldsymbol{x})$ and μ denote the (spatially varying) permeability tensor and fluid viscosity, respectively.

From the solution of the diffusivity equation (equation 3), we can obtain synthetic pressure transient data at wells that are placed in

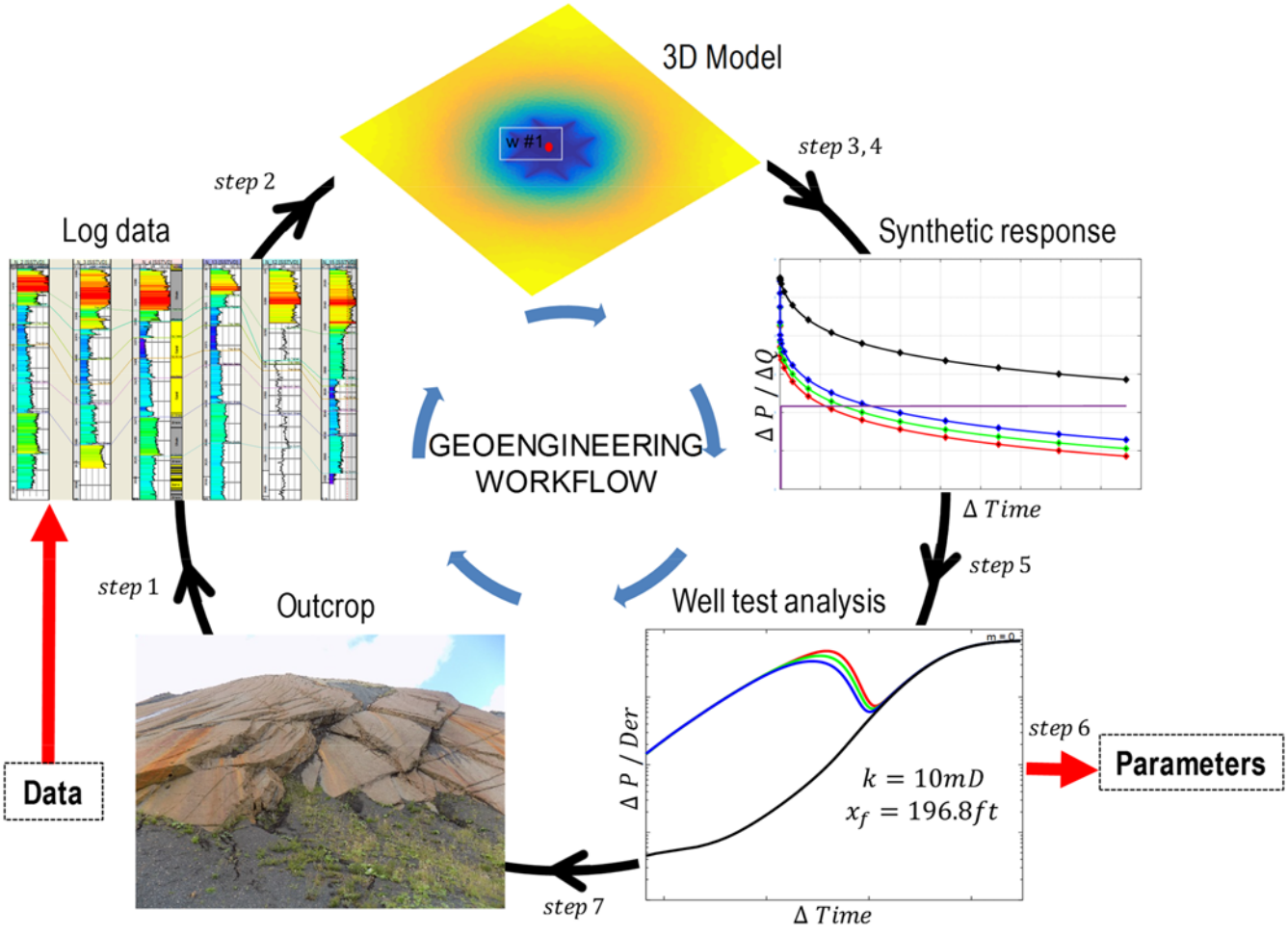

Fig. 4. Geoengineering workflow for integrated well testing (modified from Corbett *et al.* 2012).

selected locations in the reservoir. Next, we can correlate the observed pressure data to routine pressure transient analysis (PTA) with the known input parameters (e.g. fracture orientation and connectivity) in the reservoir model to understand how the dynamic reservoir behaviour is impacted by natural fractures. The workflow can be summarized in the following steps (see Fig. 4):

1. build a detailed synthetic geological model comprising a mapped fracture network (from an outcrop analogue);
2. use petrophysical properties from logs for the matrix that are representative of a subsurface reservoir.
3. represent the geological model in a reservoir-simulation model that employs unstructured grids so that the fractures can be preserved explicitly;
4. numerically simulate drawdown for a wide range of possible reservoir parameters and well locations;
5. analyse the resulting numerical pressure transient data in a well-test package for PTA;
6. estimate the effective reservoir parameters for the simulation model;
7. correlate the pressure transient to the known geological features of the reservoir model. Where analysis disagrees with model input, make necessary changes to improve performance and correlation.

We used the geoengineering workflow with the DFM approach that is available in the open-source Matlab Reservoir Simulation Toolbox (MRST) (Lie *et al.* 2012) to solve equation (3) numerically, explicitly resolve the fractures in the reservoir models and to evaluate the effect of geometrical arrangements of the fracture network, as well as well locations, on the pressure transient signals (the input files can be downloaded from: http://carbonates.hw.ac.uk). MRST offers a range of different discretization methods. Here, we employ the PErpendicular Bisector (PEBI) method, which has proven to be efficient, robust and accurate when discretizing complex realistic fracture networks (Sun *et al.* 2015). The conditions for accurate PEBI simulations are that the permeabilities are isotropic and permeability orthogonality is guaranteed. However, the main advantage of the PEBI approach is its flexibility, enabling the grids to conform to complex geometrical features, including fractures and radial gridding around the wells, whilst resolving the early time transients (Zheng *et al.* 2007).

PEBI gridding and numerical modelling

The PEBI gridding workflow used in this study is illustrated in Figure 5. Fracture traces, well locations and domain boundaries are represented in the form of linear coordinates. Edges are then delineated by creating a planar straight-line graph (PSLG) containing a set of fracture vertices and adjoining edges (Fig. 5a). The PSLG provides the input for a constrained Delaunay triangulation (Fig. 5b) that honours the original model geometry (Shewchuck 2002). The resulting triangulation forms the basis on which the complementary PEBI grid is generated, such that the centres of the PEBI cells correspond to the nodes of triangular elements (Fig. 5c). Finally, the 2D PEBI (Fig. 5d – without the drawn PSLG) grid is extruded vertically, resulting in a 2.5D reservoir simulation grid that is horizontally unstructured but vertically structured (Mallison *et al.* 2010; Lie *et al.* 2012; Sun *et al.* 2015). It is often referred to as 2.5D rather than 3D because the geology/geometry does not change in the third dimension. Throughout this work, we assume that the thickness of the formation is small compared to its lateral extent, and hence no variations in structure occur in the third dimension. Furthermore, the grid around the wells and fractures was locally refined to ensure that steep pressure gradients near wells and, in early times, near the fracture–matrix interfaces can be preserved accurately.

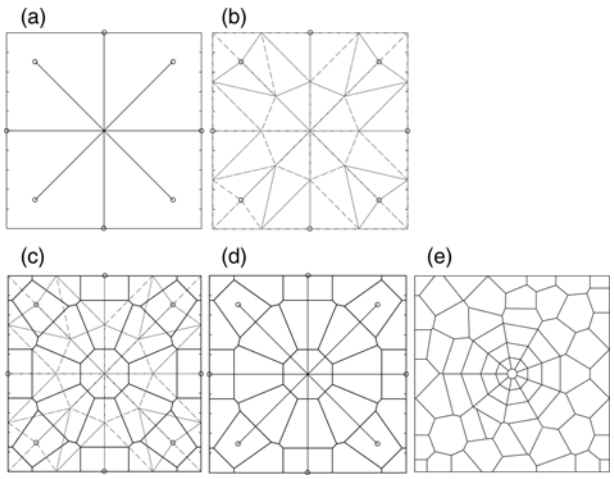

Fig. 5. Mesh generation. (**a**) Planar straight-line graph (PSLG) representing sets of fracture nodes and adjoining edges; (**b**) Delaunay triangulation (grey dash lines); (**c**) PEBI grids built around triangular mesh nodes; (**d**) resulting PEBI with respect to the initial PSLG; and (**e**) separate meshing example showing radial gridding around a well.

To enable this grid refinement, a procedure was implemented to improve the quality of the mesh at multiple fracture intersections, as well as at asymmetrical and low-angle intersections. Various approaches have been used to resolve meshing of complex geometry features, including small features, sharp angles in intersection features, multiple feature intersections or non-uniform fracture apertures (Branets *et al.* 2009; Syihab 2009; Mallison *et al.* 2010; KAPPA 2012; Olorode *et al.* 2013; Hyman *et al.* 2014; Bahrainian *et al.* 2015; Sun & Schechter 2015). Here, we developed an algorithm that involves creating a protective area where only one finite-element node is allowed at the intersection and no grid refinement is applied within this area local to the intersection (Fig. 5a–c) (this code can be downloaded from http://carbonates.hw.ac.uk). Note that the image in Figure 5d shows an improved mesh where the PEBI cell is constructed around the initial finite-element node and the adjoining cells conform to the defined fracture geometry. In addition, we applied the algorithm of Møyner & Lie (2016) to refine the grid radially around the well, especially in cases where wells are located in the matrix and close to fractures (Fig. 5e).

Once the 2.5D reservoir model is constructed, it is populated with representative subsurface petrophysical properties (step 2 in Fig. 4; Table 1), including porosity and permeability, that are used as input for flow computations. For simplicity, the reservoir matrix is assumed to be isotropic and homogeneous, so that single constant values of petrophysical properties can be used, but heterogeneous matrix properties are possible too. The fractures are assumed to be open (100% porosity), have higher permeabilities than the matrix and also have uniform properties that do not change as a function of pressure (i.e. the reservoir is stress-insensitive). Fracture

Table 1. *Reservoir model and fluid properties*

Reservoir initial pressure, p_0 (psi)	4351
Flow rate, q (bbl/day)	31.45
Matrix porosity, φ_m (fraction)	0.3
Matrix permeability, k_m (mD)	10
Fracture porosity, φ_f (fraction)	1.0
Oil viscosity, μ_o (cP)	1.0
Oil density, ρ_o (kg m^{-3})	700
Oil formation volume factor (reservoir barrels/stock tank barrels: rb/stb)	1.0
Total compressibility (psi^{-1})	6.8948×10^{-6}

permeabilities, k_f, are computed from the fracture aperture, a, using the parallel plate law: that is, $k_f = a^2/12$. To avoid infeasibly small grid cells in the fracture, we rescaled the fracture permeability and porosity, in case a fracture grid block was wider than the fracture aperture, in order to obtain the correct face transmissibility.

To ensure that numerical artefacts do not impact the simulation results, we tested how grid refinement around the fractures and well, as well as the selection of time steps, influences the numerical simulations by comparing synthetically generated pressure profiles to, and analytical solutions for, various levels of grid refinement and time steps. Based on this analysis, all models use grids that coarsen logarithmically away from the smallest geometrical feature (i.e. the grid blocks containing the fractures) and set the maximum grid-block size to be four orders of magnitude larger than the smallest grid block in the model. Simulation time steps are also increased logarithmically to ensure smooth pressure transient profiles. The simulation results were further compared, for simple orthogonal fracture patterns, to a commercial simulator (CMG IMEX).

Model validation

A number of sensitivity studies were completed to validate the accuracy of the modelling methodology, and to make sure that the pressure transient response from the reservoir reflects the physical conditions and are not impacted by numerical dispersion. For the model validation, we ran simulations for the matrix model (Table 2, Model 1 and Fig. 6), single fracture (Table 2, Model 2) and multiple intersecting (multiwing) fractures (Table 2, Model 3) models where the well is located centrally and symmetrically in the single fracture, and at a bifurcation point for multiwing fractures, respectively (see Figs 7a and 8a). The first set of results is for the homogeneous matrix models with a well located at the centre of a square reservoir block (Fig. 6). Each of the graphs in Figure 6 shows the main flow regimes (early time wellbore storage (WBS) with slope $m = 1$; radial flow with $m = 0$; and late-time PSS flow with $m = 1$, indicating boundary) and captures the sensitivities to changes in reservoir parameters (KAPPA 2012). Figure 6a shows similar pressure derivatives as a function of permeability. However, higher values of permeability deviate from pure WBS at earlier times, indicating the reservoir's ability to react faster to production. Changes in porosity (Fig. 6b) do not show changes in the stabilization of the pressure derivative (i.e. during radial flow). Deviations are observed, however, during transition from pure WBS to radial flow, and from radial flow to PSS. Given the same reservoir size and properties, changes in porosity are proportional to the time for the PSS influence to reach the well. Figure 6c shows that with changes in production rate, the derivative shifts vertically but the pressure profile remains the same. High rates produce proportionately high-pressure deviations from the initial pressure, shifting the derivative upwards. The effects of changes in viscosity on pressure derivative is opposite those described above for changes in permeability (Fig. 6a).

Next, we performed sensitivity analysis using simple fracture geometries so that our numerical model can be validated with existing analytical solutions (Bourdet 2002). Results for a close-up of the unstructured PEBI grid with refinement around a single fracture intercepted by a well (Fig. 7a) are shown in Figure 7b. From top to bottom in Figure 7b, the flow regimes identified with changes in the conductivity include bilinear flow, $m = 1/4$; linear flow, $m = 1/2$; and radial flow, $m = 0$. A detailed description of the PTA of a single fracture model is provided later in the section 'Simulation results and observations'. Figure 8a shows a close-up of the unstructured PEBI grid with refinement around multiwing fractures used to further validate our model. The results (Fig. 8b) showing changes in pressure (dashed lines) and the corresponding pressure derivatives (solid lines) for different values of asymmetry factors (AFs) indicate

Table 2. *Summary of simulation models with grid dimensions and well locations*

Model name	Well location	Model description and dimension
Model 1: Unfractured (matrix) model	Matrix	200 × 200 × 1 m homogeneous matrix model used for validation and sensitivities study
Model 2: Single fracture model	Fracture	200 × 200 × 1 m homogeneous matrix model with a two-wing (single) fracture used for validation. F_{cD} of 1:500
Model 3: Multiple intersection (multiwings) fracture model	Fracture	200 × 200 × 1 m homogeneous matrix model with six-wing (multiple) fractures and asymmetrical factors used for validation. F_{cD} of 10
Model 4a: Idealized connected fracture network	Fracture	4 km × 4 km × 1 m homogeneous matrix model with an idealized connected fracture network. F_{cD} of 0.1–10 000
Model 4b: Idealized connected fracture network	Matrix	4 km × 4 km × 1 m homogeneous matrix model with an idealized connected fracture network. F_{cD} of 0.1–10 000
Model 5a: Idealized disconnected fracture network	Fracture	4 km × 4 km × 1 m homogeneous matrix model with an idealized disconnected fracture network. F_{cD} of 0.1–1000
Model 5b: Idealized disconnected fracture network	Matrix	4 km × 4 km × 1 m homogeneous matrix model with an idealized disconnected fracture network. F_{cD} of 0.1–1000
Model 6a: Outcrop example of connected fracture network	Fracture	550 × 550 × 1 m homogeneous matrix subset-model with a realistic outcrop connected fracture patterns. F_{cD} of 0.1–10
Model 6b: Outcrop example of connected fracture network	Matrix	550 × 550 × 1 m homogeneous matrix subset-model with a realistic outcrop connected fracture patterns. F_{cD} of 0.1–10
Model 7a: Outcrop example of disconnected fracture network	Fracture	480 × 450 × 1 m homogeneous matrix subset-model with a realistic outcrop disconnected fracture patterns. F_{cD} of 0.1–10
Model 7b: Outcrop example of disconnected fracture network	Matrix	480 × 450 × 1 m homogeneous matrix subset-model with a realistic outcrop disconnected fracture patterns. F_{cD} of 0.1–10
Model 8: Idealized connected fracture network with small fractures	Fracture	4 km × 4 km × 1 m homogeneous matrix model with an idealized connected fracture network and (un)connected small fractures. F_{cD} of 1000
Model 9: Idealized disconnected fracture network with small fractures	Fracture	4 km × 4 km × 1 m homogeneous matrix model with an idealized disconnected fracture network and (un)connected small fractures. F_{cD} of 1000
Model 10: Idealized disconnected fracture network with increasing small fracture	Fracture	4 km × 4 km × 1 m homogeneous matrix model with an idealized disconnected fracture network and different lengths of unconnected small fracture. F_{cD} of 1000

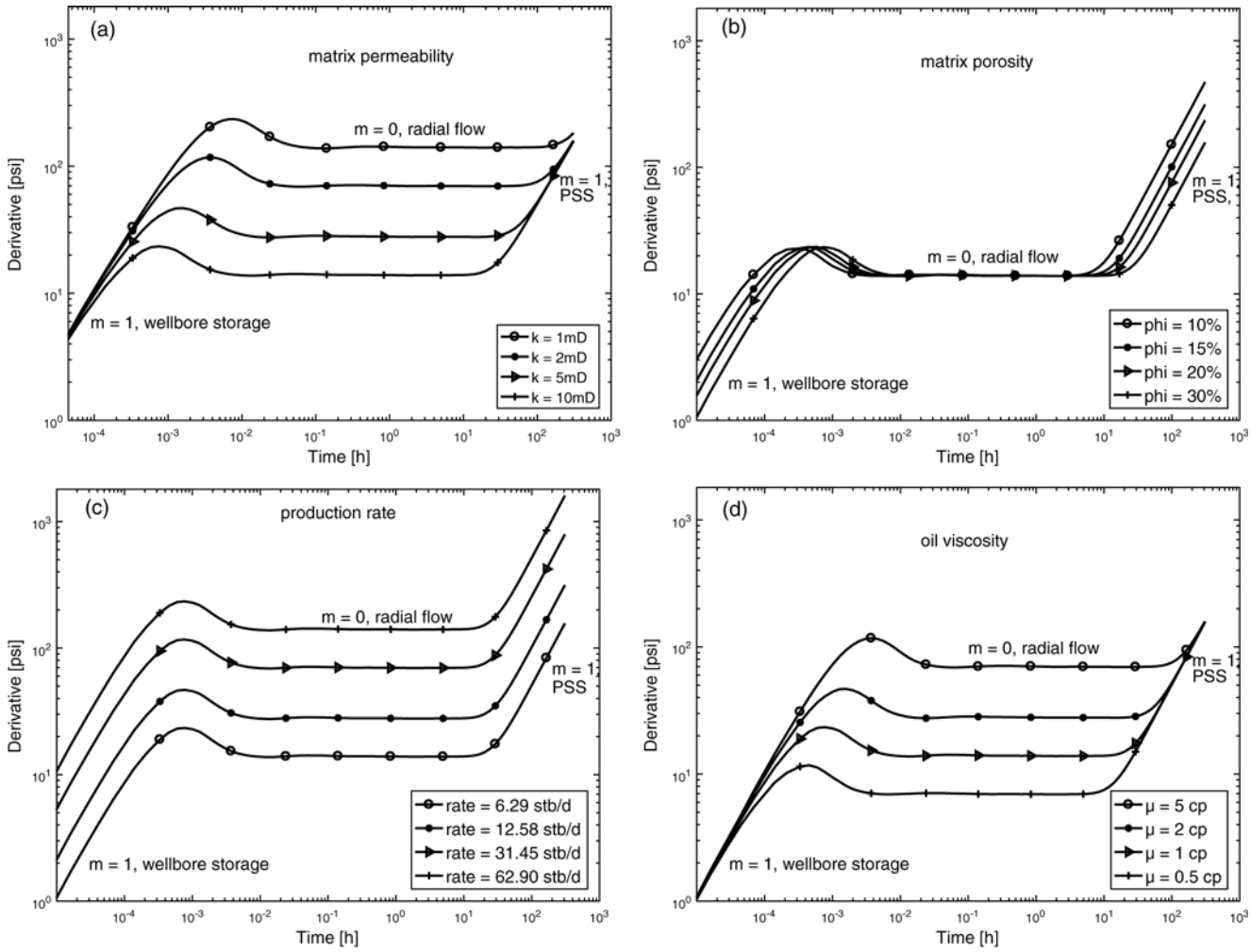

Fig. 6. Un-fractured (matrix) model sensitivities. (**a**) Matrix permeability; (**b**) matrix porosity; (**c**) production rate; and (**d**) oil viscosity. stb/d, stock tank barrel per day.

similar responses to those in the analytical and semi-analytical solutions of Berumen *et al.* (2000) and Wanjing & Changfu (2014), respectively. The AF measures the well offset from the centre of the fracture. Our simulation results were also validated using CMG IMEX for simple orthogonal fracture patterns. The validation models further provide references for the interpretation of the more complex fracture geometries simulated later.

In all simulation models, a jacket of matrix cells with uniform properties is added to prevent flow in the fractures from interacting with the model boundary (Aljuboori *et al.* 2015). Since the fracture

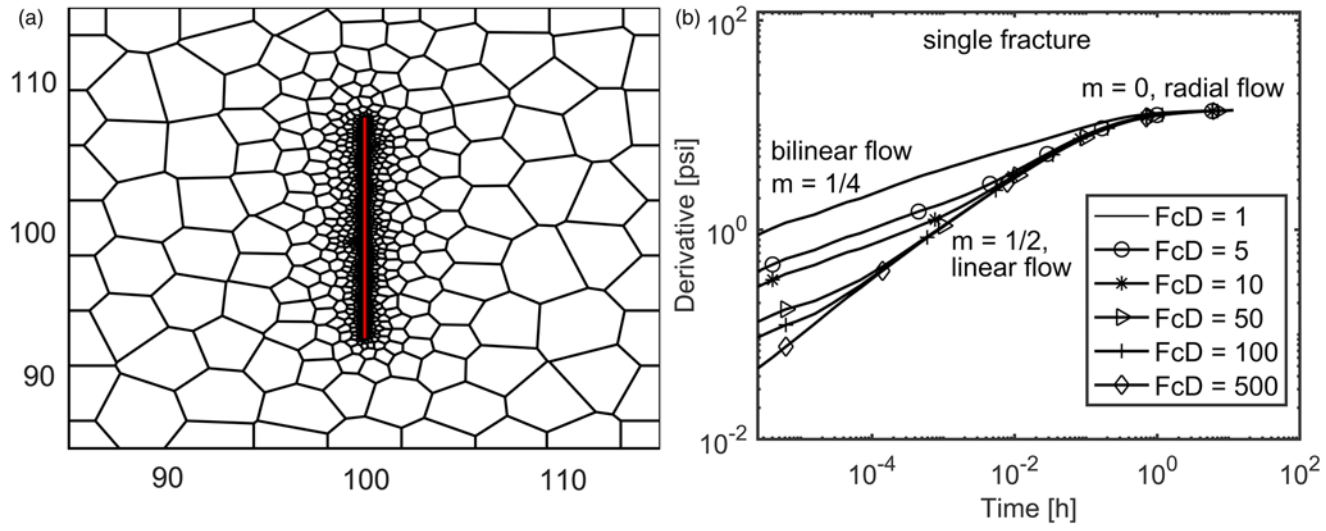

Fig. 7. Single fracture model. (**a**) Close-up of the unstructured PEBI grid with refinement around a single fracture; and (**b**) simulated results with variable fracture conductivities (FcD of 1–500). FcD denotes the dimensionless fracture conductivity, as defined in equation (4).

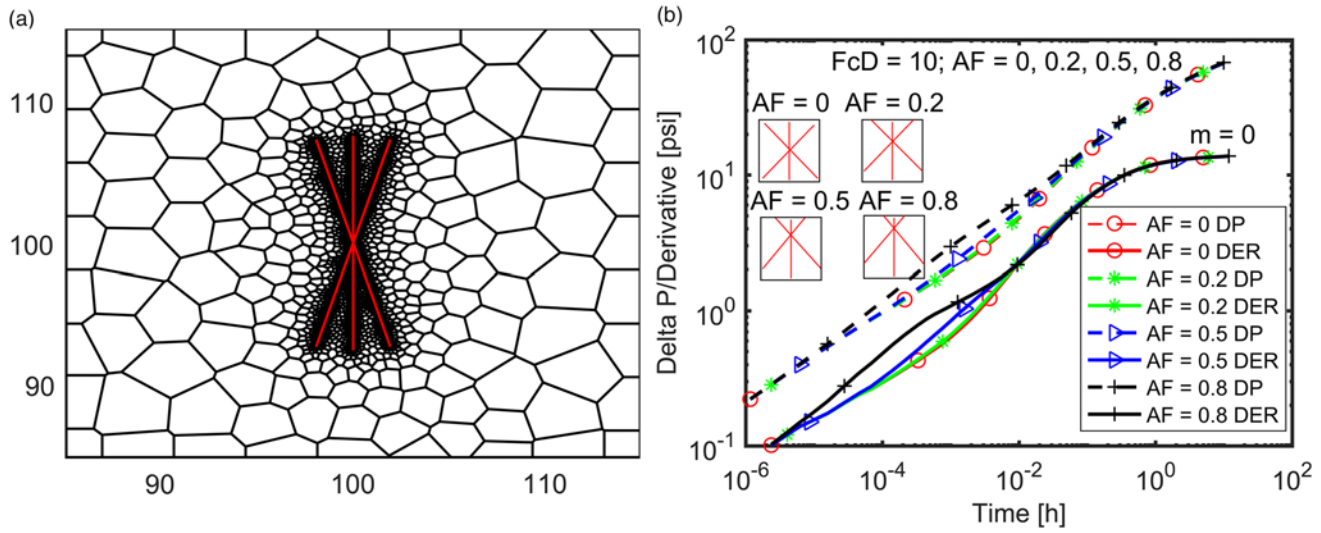

Fig. 8. Multiwing fractures model. (**a**) Close-up of the unstructured PEBI grid with refinement around the multiwing fractures; and (**b**) simulated results with FcD values of 10 and AF values of 0–0.8. The dashed lines and solid lines show changes in pressure and the corresponding pressure derivatives, respectively. The asymmetry factor, AF, measures the well offset from the centre of the fracture.

cells are characterized with a high permeability, the pressure response in this medium can propagate very quickly to the model boundary even before the effect of exchange between fractures and the matrix has started. Therefore, it is necessary to prevent the late-time boundary effect from interfering with the middle-time pressure transient response in our simulations.

Outcrop data and other input parameters

The approach of this study is applied to a real outcrop of fracture networks (Fig. 9) obtained from the Turonian–Campanian Jandaira carbonate formation, which crops out in large parts of the Potiguar Basin in NE Brazil (Bertotti *et al.* 2017; de Graaf *et al.* 2017). The Jandaira Formation is a subhorizontal formation, dipping on average 3° towards the north, creating exposed pavements with dimensions exceeding several hundred by several hundred metres. These exposures are ideal for multiscale fracture-network characterization. Using satellite imagery in combination with drone images and conventional outcrop measurements, more than 18 000 fractures have been mapped in pavements throughout the basin (Bisdom *et al.* 2017*a*).

Although layers with folds and faults are relatively rare, the Jandaira Formation is intensely fractured. Based on cross-cutting relationships between vertical fractures and burial-related horizontal stylolites, and the abundance of bed-perpendicular conjugate sets of fractures, most of the fractures are interpreted to have formed at shallow depths during a relatively early phase of burial (Bertotti *et al.* 2017). Outcrop and thin-section analyses of fracture infill show that fractures have shear and opening components, indicating that these are hybrid fractures (Ramsey & Chester 2004; Bertotti *et al.* 2017). The main driving mechanism for fracturing was regional shortening, under a maximum horizontal stress orientated north–south to NE–SW (Bertotti *et al.* 2017; de Graaf *et al.* 2017). As a result, most fractures are orientated north–south and NE–SW, dipping perpendicular to bedding (Bisdom *et al.* 2017*a*).

The east–west-striking features are barren in the outcrops but, prior to exhumation, they were tectonic (i.e. bed-perpendicular) stylolites formed in the same north–south to NE–SW regional shortening phase as the fractures (Bertotti *et al.* 2017). Fractures from different orientation families are observed to be mutually cross-cutting, providing further evidence for their simultaneous formation. The only hierarchy that is observed in some outcrops is related to fracture size, as smaller fractures terminate against larger fractures.

These burial-related fractures are present at high densities throughout the entire basin, even though there is only limited seismic-scale deformation. These patterns have furthermore been formed under relatively low stresses. There are many carbonate reservoirs that have a similar lack of seismic-scale deformation, where conventional methods, such as curvature analysis, do not indicate significant fracturing, but the studies of the Jandaira Formation show that high-density fracture patterns may still exist. For this type of fracture network, there is significant value in having the ability to identify fracture flow from well-test data.

Fractures from one of the Jandaira pavements are used in this study (Fig. 9). This 400 × 175 m pavement has been imaged using a drone, resulting in a georeferenced image from which nearly 2000 fractures were mapped using GIS software (Bisdom *et al.* 2017*b*). Fracture lengths in this pavement range from 0.68 m to about 90 m with apertures observed at the outcrop ranging from <0.1 mm up to 10 mm (Bisdom *et al.* 2016). Bertotti *et al.* (2014) noted that, even though the orientation of the structures is preserved, fracture apertures observed in the outcrop are not representative of the subsurface conditions and, hence, we consider variable fracture apertures in our sensitivity study. Like the Jandaira Formation, recent karstification has altered the fracture/joint properties at the surface of the outcrop example shown in Figure 1a. For this reason, subsurface model parameters are selected in this paper – rather than being measured in the field – with the contrast between matrix and fracture permeability being the important consideration. The variations in fracture density observed in the outcrop in Figure 9 allowed us to evaluate how pressure transients evolve when wells are located in different parts of the fracture network and where the dual-porosity model is valid to interpret the pressure transients. The two insets in Figure 9 indicate locations where smaller-scale models of fracture patterns are taken to simulate disconnected and connected fractures, respectively. The upper inset represents the disconnected fracture network, and the lower one the connected fracture network.

The reservoir and fluid properties used in this study are summarized in Table 1. For simplicity, all simulations assume single-phase laminar flow, no gravity effects, a homogenous and isotropic reservoir matrix with uniform thickness, uniform fracture aperture with a single porosity and permeability for the entire fracture network. We also assume layer-bound fractures and, hence, represent the model with the third dimension as a single layer. Wells are orientated vertically and fully penetrate the formation and

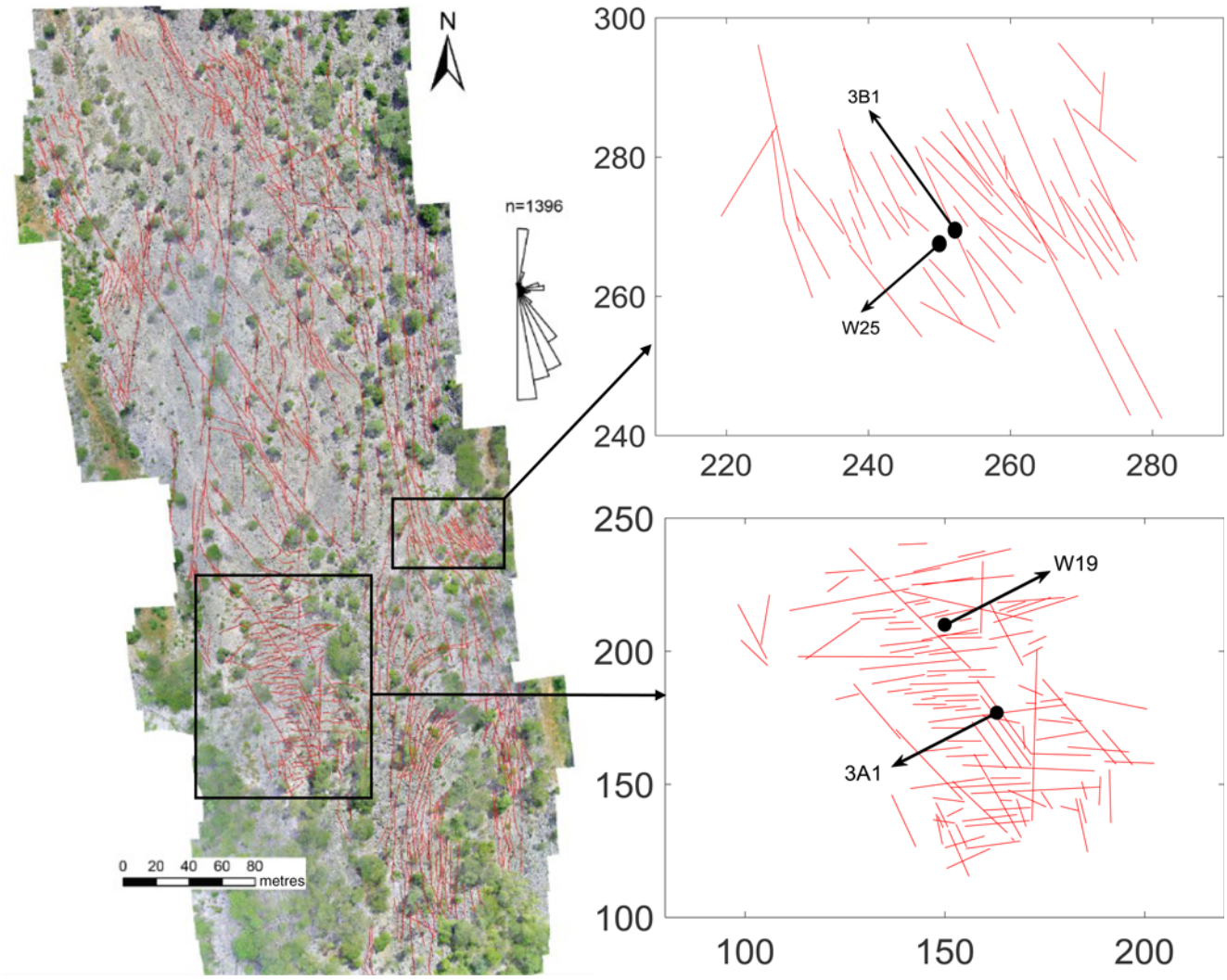

Fig. 9. Aerial view of the fracture patterns in the Jandaira Formation, Brazil (left) (Bisdom 2016). The marked inset boxes indicate the locations where subset-model fractures patterns are taken. The upper inset represents a disconnected fracture and network, and the lower inset is for connected fracture network.

produce at a constant rate for any given simulation. Table 2 summarizes all simulation scenarios.

Dimensionless variables

In this study, the following dimensionless numbers are used to compare and quantify the reservoir properties in the different simulations.

Dimensionless fracture conductivity:

$$F_{CD} = \frac{k_f a}{k_m l_w} \tag{4}$$

Dimensionless pressure:

$$p_D = \frac{k_m h}{141.2 q \mu}[p_0 - p_{wf}(t)] \tag{5}$$

Dimensionless time:

$$t_D = \frac{0.0002637 k_m t}{\mu \varphi_m (C_t)_m l_w^2} \tag{6}$$

In these equations, F_{CD} and l_w denote the dimensionless fracture conductivity and fracture half-length (measured in ft), respectively; h denotes the reservoir thickness (in ft); q denotes the rate of production (in stock tank barrels per day (STB/day)); p_0 and p_{wf} denote the initial pressure and flowing well pressure (in psi); t denotes time (in h); and μ and $(C_t)_m$ denote viscosity (in cP) and total matrix compressibility (in psi^{-1}), respectively. Constants are conversion factors from SI units to customary field units.

Simulation results and observations

Single fracture model

Our simulation and interpretation of well-test signals in a NFR starts with a reservoir model containing a single natural fracture that intersects the well (Fig. 7), as well as a single fracture located in the matrix at different distances from the well. Although such a model is unrealistic for a real reservoir condition, it allows us to apply analytical solutions (Bourdet 2002; Kuchuk & Biryukov 2015) and provide an important reference when interpreting pressure transient behaviour for complex cases.

These reference simulations show the well-studied flow regimes for different fracture conductivities and locations of the well with respect to the fracture: for example, low fracture conductivity (up to $F_{cD} = 100$) for a well-intersecting fracture, the first flow regime observed in the pressure derivative is bilinear flow, as shown in Figure 7(b). As fracture conductivity increases to $F_{cD} = 500$ (Fig. 7b), the bilinear flow diminishes and linear flow emerges as the first flow regime before radial flow is attained (Gringarten *et al.* 1974, 1975; Cinco-Ley & Samaniego 1981; Wong *et al.* 1986;

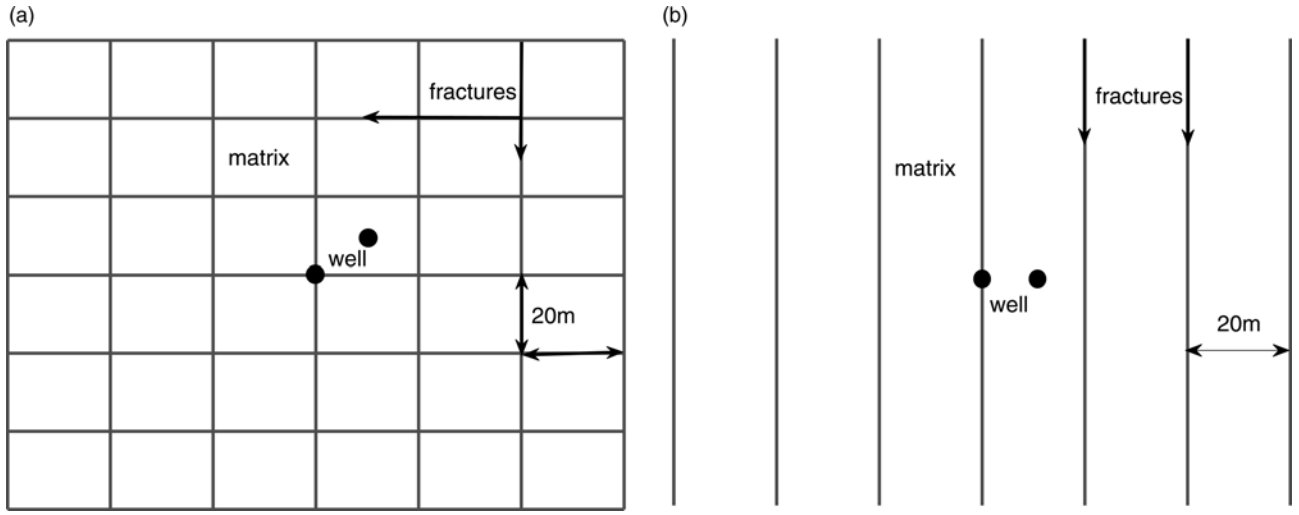

Fig. 10. Idealized fracture network with a 60 m half-length. (**a**) A connected fracture network with well-intersecting fractures and located in the matrix adjacent to fractures; and (**b**) a disconnected fracture network with similar well configurations to (a).

Bourdet 2002). This is not the case for the same reservoir and fracture properties where the well is located in the matrix (Fig. 6). It is well understood that a well located near a single fracture first shows the effect of wellbore storage followed by radial flow in the matrix (depending on the distance of the nearby fracture) and then a minimum (dip) on the derivative reflecting the period of depletion from the fracture (Cinco-Ley *et al.* 1976; Abbaszadeh & Cinco-Ley 1995). Other simulation results of a well located in the matrix adjacent to fractures are presented in Figures 10b, 11b, 12b, 13b and 14b.

In order to assess the validity and limitations of the Warren & Root (1963) dual-porosity model in the interpretation of NFRs, we first simulate a number of models containing an idealized and regular fracture network (Fig. 10). We consider two different scenarios (Table 2, models 4 and 5): a connected fracture model (Fig. 10a) that consists of uniform rectangular parallelepipeds ($20 \times 20 \times 1$ m) of matrix blocks that are separated by two sets of perfectly orthogonal fractures; and, secondly, we consider a disconnected fracture model (Fig. 10b) that has the same properties as the connected model except that it contains only a single set of parallel fractures. In each of these models, we consider both a well intersecting fracture(s) (Table 2, models 4a and 5a) and a well located in the matrix (Table 2, models 4b and 5b). In all cases, the well is located in the centre of the model or slightly offset from the centre (Fig. 10), if the well is not intersecting a fracture. We consider fracture conductivities from 60 to 6×10^6 mD m, which yield dimensionless fracture conductivities of 0.1–10 000. Table 2 contains further descriptions of the simulation models used here.

Connected and disconnected fracture networks

Figure 11 shows the resulting pressure derivatives for the connected fracture network. For the situation where a well intersects fractures (Fig. 11a), the bilinear fracture flow regime ($m = 1/4$) is observed at an early time when the fracture conductivities are low ($F_{cD} = 0.1-1$). This regime then transitions through different periods until it reaches pseudo-radial flow when equilibrium between the matrix and fracture flow is reached. However, surprisingly, as fracture conductivity increases ($F_{cD} > 10$) the typical V-shape (or 'dual-porosity dip') signature cannot be observed. The presence of well-connected fractures only produces a slanted S-shaped derivative profile, as shown by the solid line plots in Figure 11a.

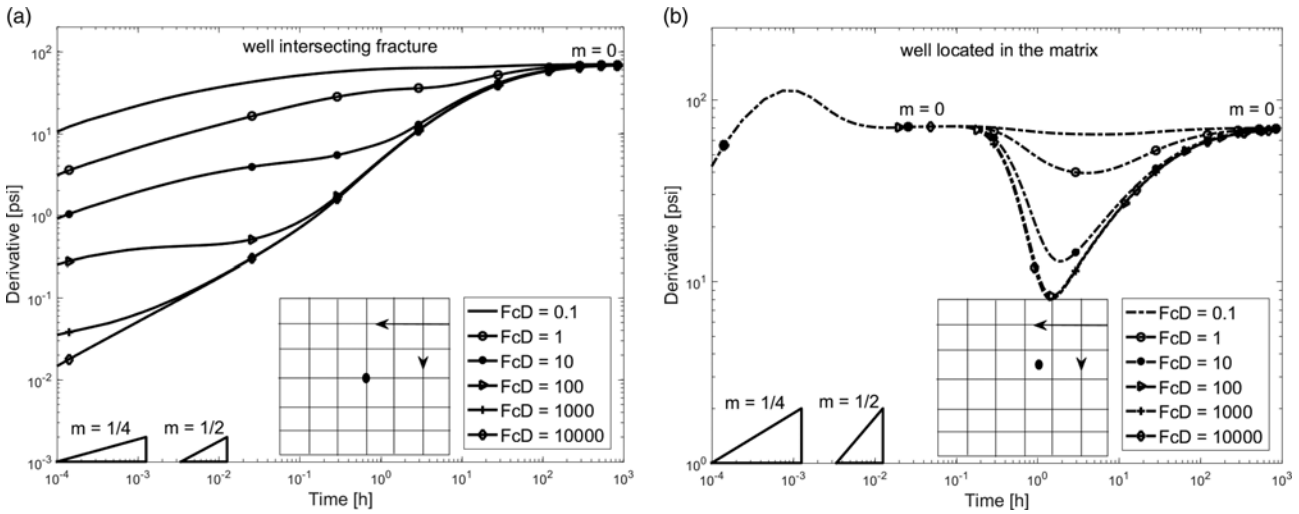

Fig. 11. Simulated pressure derivatives of an idealized connected fracture network that resembles the classical Warren & Root (1963) dual-porosity model in 2D. (**a**) Wellbore intersecting fractures and (**b**) a wellbore located in the matrix adjacent to fractures. *m* indicates the slope of the pressure derivative. Note that a slope, *m*, of 0 shows radial flow or pseudo-radial flow; *m* of 1/2 shows formation linear flow; and *m* of 1/4 shows bilinear flow.

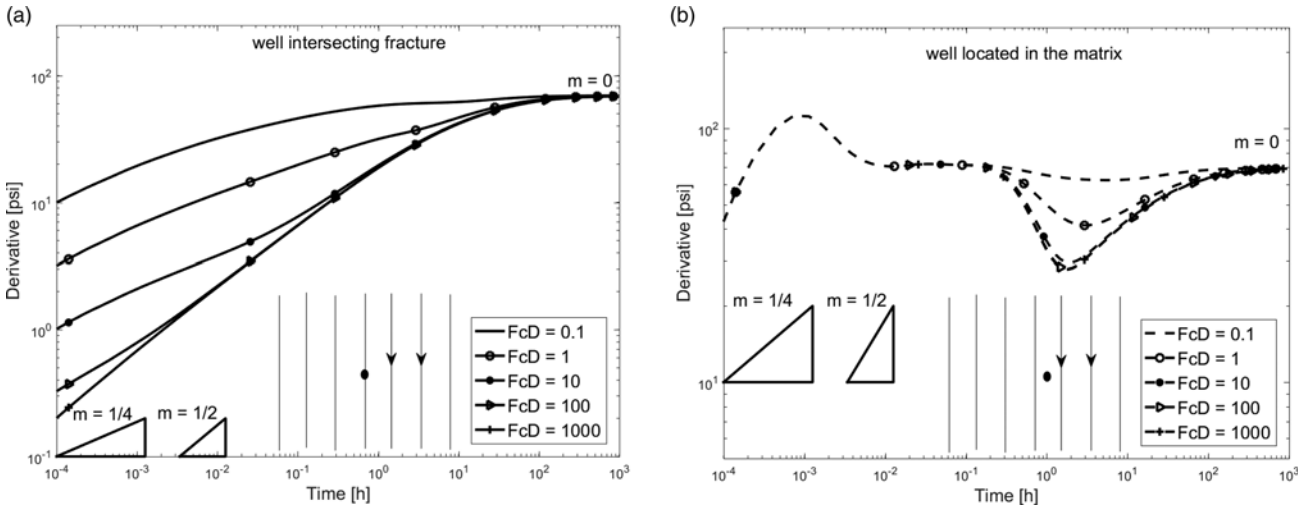

Fig. 12. Simulated pressure derivatives of an idealized disconnected fracture network with variable dimensionless fracture conductivities. (**a**) Wellbore intersecting fractures and (**b**) a wellbore located in the matrix adjacent to fractures. *m* indicates the slope of the pressure derivative. Note that a slope, *m*, of 0 shows radial or pseudo-radial flow; *m* of 1/2 shows formation linear flow; and *m* of 1/4 shows bilinear flow.

In contrast, the typical V-shape can only be observed in models where the well is not intersecting any fractures (Fig. 11b). Here, the pressure derivatives are characterized by two stabilization periods where radial flow occurs separated by transition periods which cause troughs in the derivative plots. Initially, until the first period of radial flow ($m = 0$) commences, the typical flow regimes are of a homogeneous reservoir with the well located in the matrix. So until this period, the depletion is only from the matrix without a contribution from the fractures. This is followed by a transition period (V-shape) where the contribution from the fractures becomes significant, and the matrix and fracture pressure reach equilibrium. Once the two media equilibrate, the second pseudo-radial flow ($m = 0$) is observed. For the very low fracture conductivity ($F_{cD} < 1$), the dual-porosity behaviour is apparent via a broader, U-shaped, drop in the derivative. If $F_{cD} > 10$, the classical V-shape followed by a linear flow regime is observed before the derivatives increase rapidly as the stabilization between the two systems is reached.

Figure 12a shows the simulated pressure derivatives for the disconnected fracture network. For the case where the well is intersecting a fracture (Fig. 12a), fractures with low conductivity ($F_{cD} < 100$) lead to a pressure derivative that indicates clear bilinear flow, resulting in a slope of $m = 1/4$, before a period of pseudo-radial flow emerges. With an increase in fracture conductivity ($F_{cD} = 500$), a period of linear flow of $m = 1/2$ is followed by a bilinear flow regime and, eventually, pseudo-radial flow. From the slope of the linear flow regime, the fracture half-length can be estimated. In these cases, none of the pressure transients show a dual-porosity signature. However, if the well does not intersect any fractures (Fig. 12b), the dual-porosity behaviour is in many ways similar to the connected network shown in Figure 11b, independently of the fracture conductivity.

With the insights gained from the simple orthogonal fracture geometries discussed above, we simulated the pressure transient behaviour for the natural fracture patterns observed in the Jandaira Formation (Fig. 9). We identified locations with connected fractures (Fig. 9, lower inset; see the further description in Table 2, models 6a and b) and disconnected fracture patterns (Fig. 9, upper inset; see the further description in Table 2, models 7a and b) in the outcrop data and constructed models accordingly (Figs 13 and 14). This allowed

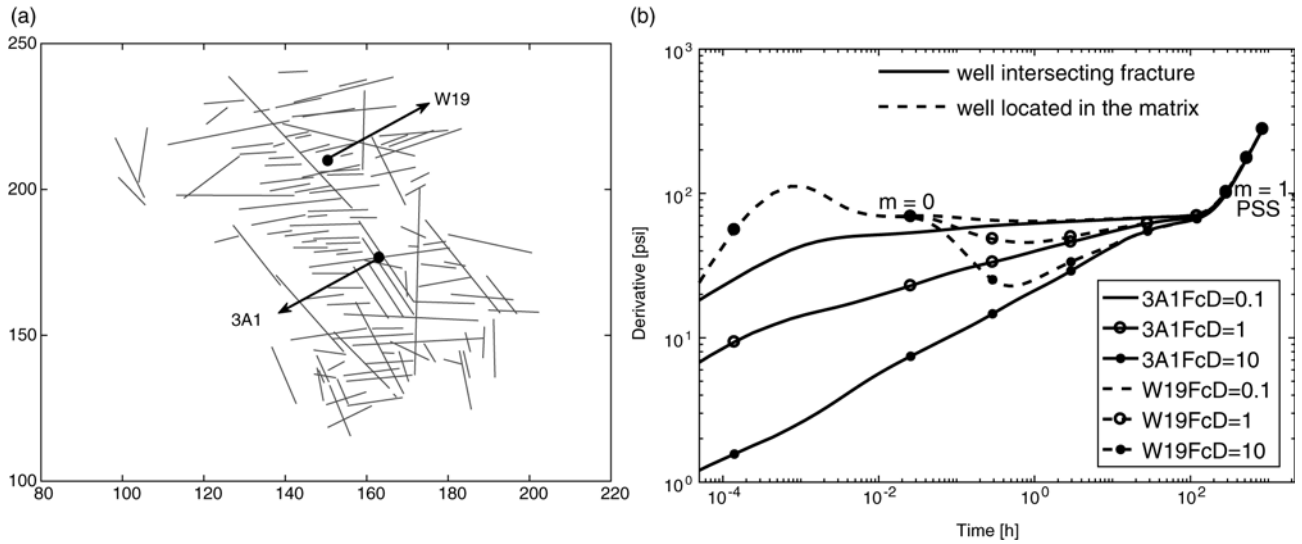

Fig. 13. Model of a connected fracture network located in the Jandaira Formation (Fig. 9, lower inset). (**a**) Fracture network with the locations of wells (the unit is in metres) and (**b**) simulated pressure derivatives. Solid lines represent simulations for well-intersecting fractures; and dashed lines are for a well located in the matrix. Note that a slope, *m*, of 0 shows radial flow, and *m* of 1 shows the reservoir boundary.

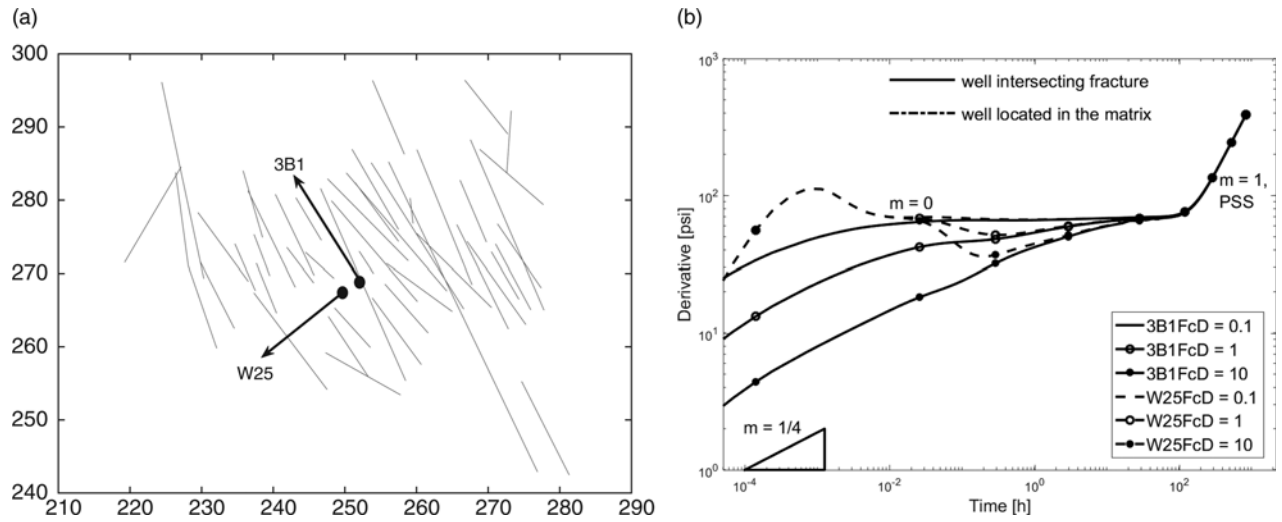

Fig. 14. Model of a disconnected fracture network located in the Jandaira Formation (Fig. 9, upper inset). (**a**) fracture network with locations of wells (the unit is in metres) and (**b**) simulated pressure derivatives. Solid lines represent simulations for well-intersecting fractures; and dashed lines are for a well located in the matrix. Note that a slope, *m*, of 0 shows radial flow; *m* of 1 shows the reservoir boundary; and *m* of 1/4 shows bilinear flow.

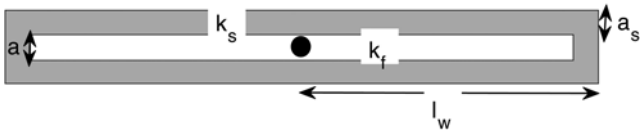

Fig. 15. Diagram illustrating the fracture skin surrounding a single fracture penetrated by a wellbore at half-length, l_w. a, k_f, a_s and k_s denote the fracture aperture, fracture permeability, damage (skin) zone aperture and skin zone permeability, respectively.

us to compare the pressure transient behaviour observed for the idealized fracture pattern to the transient behaviour in more realistic fracture patterns. As in the simulations depicted in Figures 11 and 12, we ran simulations for wells intersecting a fracture and wells that are located in the matrix. Figures 13 and 14 show that the pressure transients for the realistic, outcrop-based fracture networks are similar to those in the idealized fracture systems. Again, the dual-porosity signature is only apparent if the well is located in the matrix, not intersecting a fracture (as shown by the dashed lines in Figs 13b and 14b).

Effect of fracture skin

A key observation is the counter-intuitive behaviour of the dual-porosity signal. It can only be observed if the well is located in the matrix, even in situations where the fractures are well connected. This is in contrast to the underlying theory of the Warren & Root (1963) dual-porosity model. Previous studies (e.g. Cinco-Ley & Samaniego 1977; Cinco-Ley *et al.* 1985; Gringarten 1987; Bourdet 2002; Kuchuk & Biryukov 2015) have discussed that the type of interporosity flow between the matrix and the fractures which is assumed in a computation impacts the presence or absence of the dual-porosity signature, depending on whether the well is intersected by fractures or not. The above studies classified dual-porosity solutions into restricted interporosity flow and unrestricted interporosity flow. The restricted interporosity flow solution relates the dual-porosity behaviour to the presence of a skin at the fracture surface (Cinco-Ley & Samaniego 1977) and/or within fractures (Cinco-Ley & Samaniego 1981) (i.e. damage caused by the presence of minerals, filter cake, polymer-invaded zone, etc.) that restricted communications between the matrix and the fractures or within fractures. The presence of the interporosity skin causes the

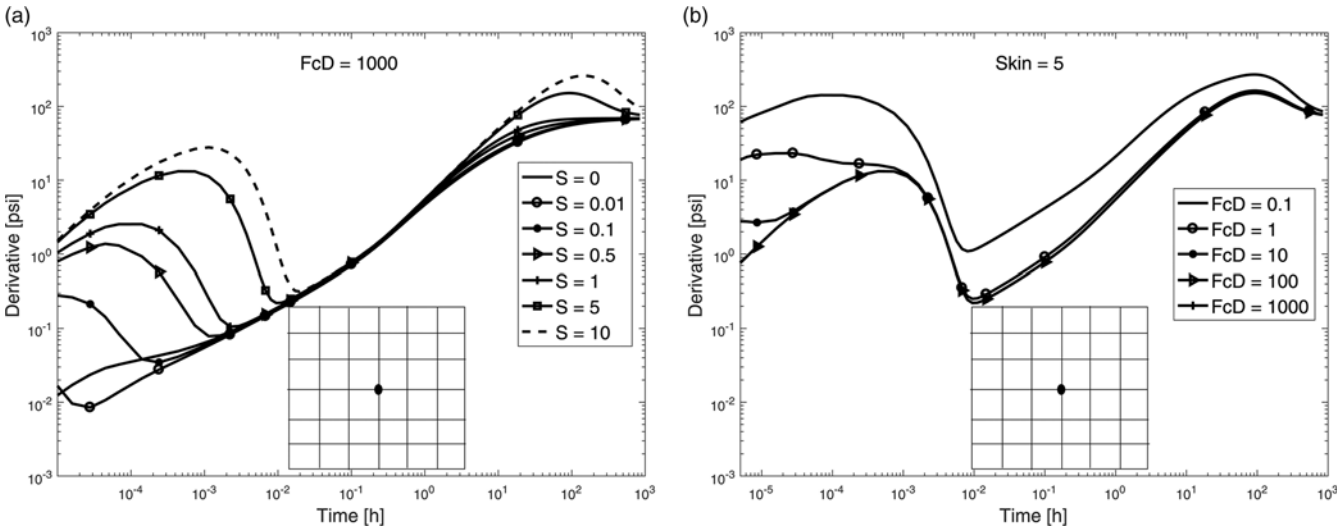

Fig. 16. Simulated pressure derivatives of a fracture-intersecting well in an idealized connected fracture network. (**a**) Variable skin (*S* of 0–10) with FcD of 1000 and (**b**) constant skin of 5 with variable fracture conductivities (FcD of 0.1–1000).

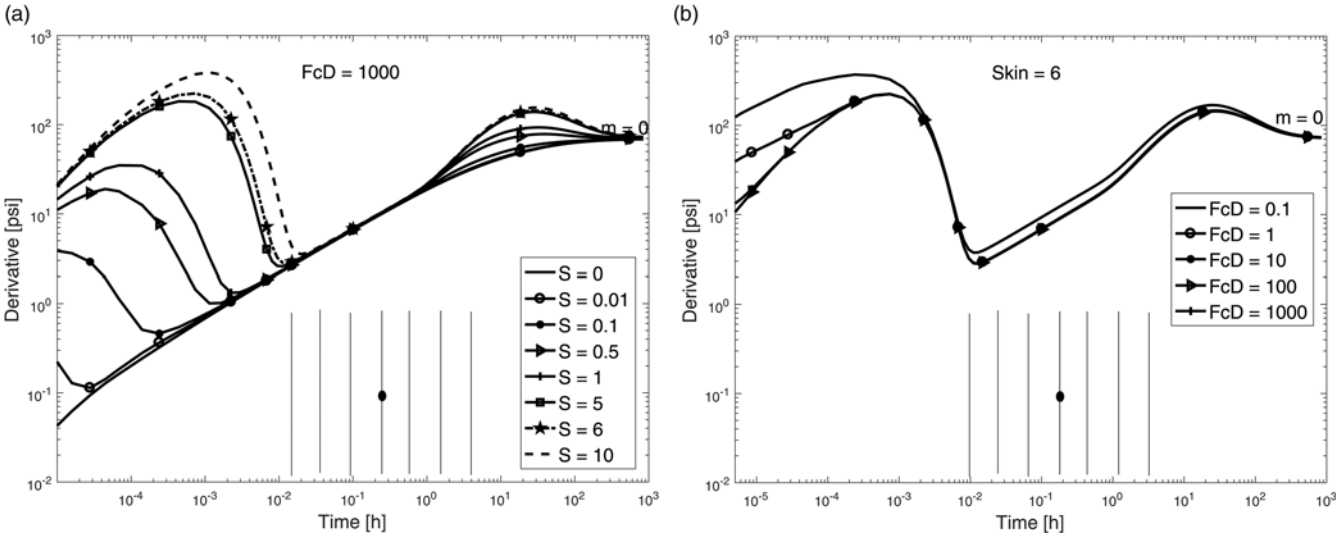

Fig. 17. Simulated pressure derivatives of a fracture-intersecting well in an idealized disconnected fracture network. (**a**) Variable skin (S of 0–10) with FcD of 1000, and (**b**) constant skin of 6 with variable fracture conductivities (FcD of 0.1–1000).

resulting pressure transient behaviour for a TIF model to show a dual-porosity V-shape similar to PSSIF (Valdes-Perez *et al.* 2011). The unrestricted interporosity flow is the same as the TIF model without taking any form of interporosity skin into account.

All of the results presented so far in this paper relate to the unrestricted interporosity flow. This is because our model assumes simulation under TIF conditions and does not contain any interporosity skin that restrict flow within fractures or between matrix and fracture. No dual-porosity response is observed for a well intercepting fractures under TIF. To account for restricted interporosity flow (i.e. TIF plus interporosity skin), we therefore have modified the model and simulated for a well that is intersecting fractures with fracture damage (skin). The relationship between fracture skin and other reservoir properties is modelled after Cinco-Ley & Samaniego (1977) (see Fig. 15) and is defined as follows:

$$s_f = \frac{\pi a_s}{2l_w}\left(\frac{k}{k_s} - 1\right) \tag{7}$$

where s_f, a_s and k_s denote fracture skin, width and permeability of skin zone, respectively. Other parameters remain as previously defined. As before, we first explore the impact of fracture skin on the idealized connected and disconnected fracture networks before we proceed to model the more complex fracture geometries. The fracture skin was varied from 0 to 10 by assigning the corresponding value of the permeability of the skin zone.

Figures 16 and 17 show the effect of fracture skin for the connected and disconnected fracture networks, respectively. A key observation is that a higher positive fracture skin (i.e. more fracture damage) leads to more obvious dual-porosity responses. This behaviour is particularly prominent for a high fracture skin ($S \geq 5$) that locally restricts flow between fracture and matrix, although the permeability contrast between the fractures and matrix remains very low. It is clear that the dual-porosity signature is a result of the skin effect (i.e. the restricted interporosity flow) rather than an effect of the well located in the fractures. Under this flow condition, the initial depletion from a fractured reservoir with skin emanates only from the fracture system; the discharge from the surrounding matrix is choked because of the reduction in permeability between the fractures and the matrix. This condition could allow flow from the fractures to stabilize and the transition period then only follows after the flow from the matrix overcomes the barrier created by the fracture skin.

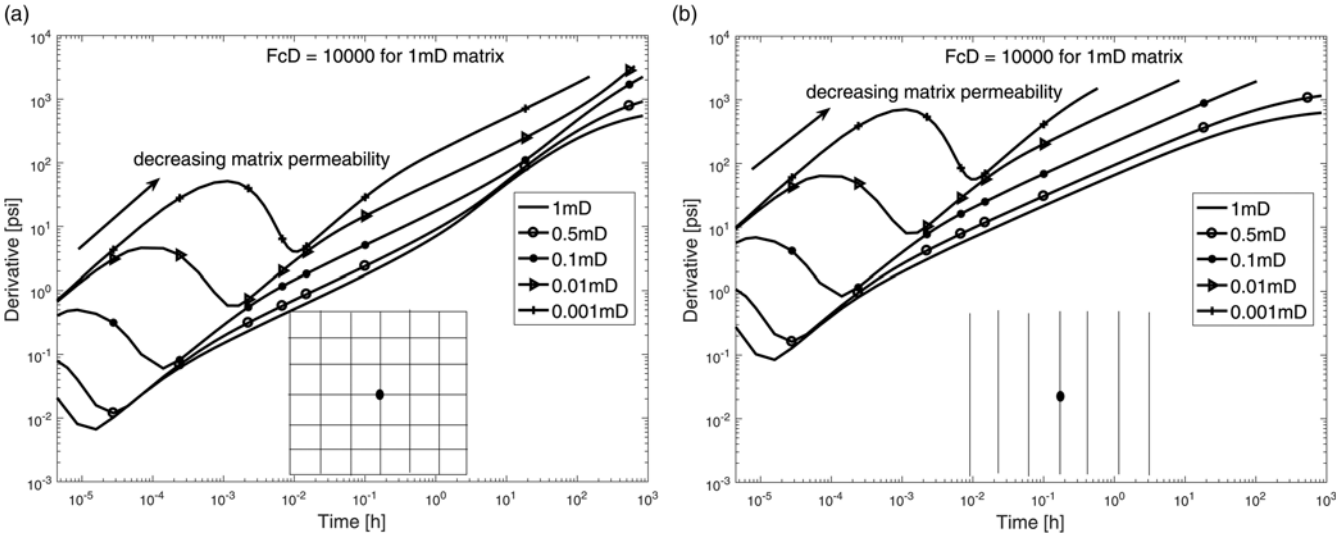

Fig. 18. Simulated pressure derivatives of well-intersecting fractures in idealized fracture networks with a matrix permeability ranging from 1 to 0.001 mD for a connected fracture network (**a**) and disconnected fractures (**b**).

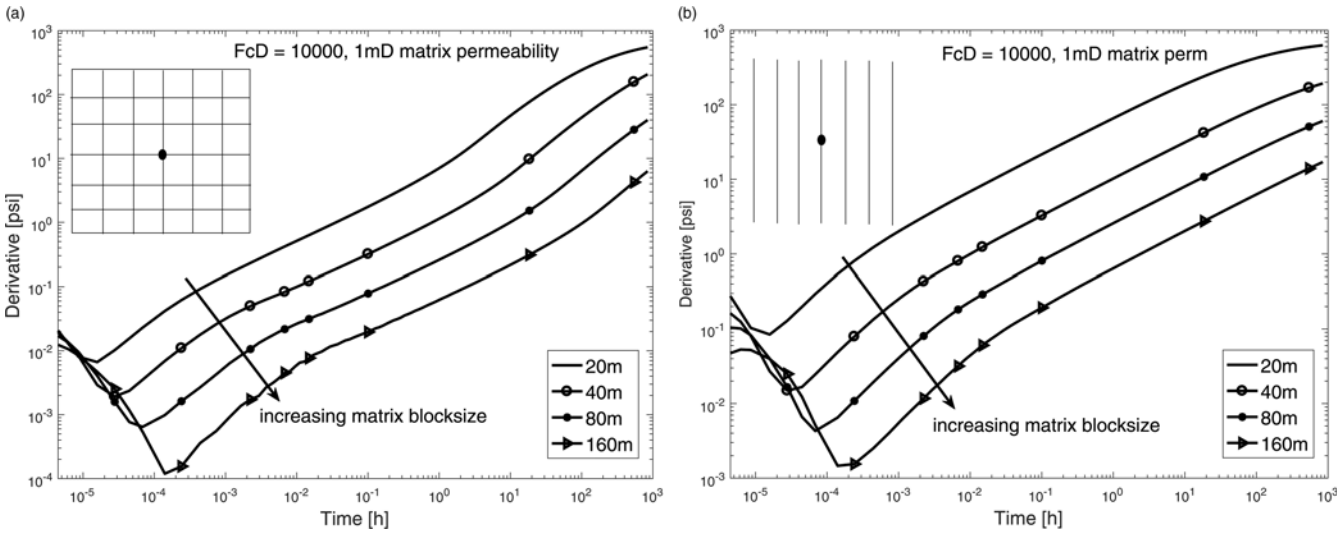

Fig. 19. Simulated pressure derivatives of well-intersecting fracture(s) in idealized fracture networks with increasing matrix block size from 20 to 160 m at a constant matrix permeability of 1 mD for a connected fracture network (**a**) and disconnected fractures (**b**).

Effect of matrix permeability

The fact that restricted interporosity flow can cause a clear dual-porosity signature raises the question of whether unrestricted interporosity flow could also show a dual-porosity signature if the matrix permeability is reduced. To test this, we kept the fracture permeability constant and successively reduced the matrix permeability, rather than changing F_{cD} by keeping the matrix permeability constant and changing the fracture permeability. This still results in the same fracture permeability values, but there will be less flow in the matrix; this configuration is in agreement with one of the key assumption in the Warren & Root (1963) model, which only considers situations where flow within the matrix is negligibly small.

Figure 18 shows the pressure transients for the idealized fracture networks with decreasing matrix permeability. In both the connected network (Fig. 18a) and the disconnected network (Fig. 18b), the dual-porosity signature becomes more prominent with decreasing matrix permeability. The reason for this response is similar to the restricted interporosity flow (Figs 16 and 17) in that the fluid exchange between the fracture and matrix is reduced. However, since there is no fracture skin, the flow behaviour still falls into the category of unrestricted interporosity flow. There are two important observations. First, the matrix permeability must be below 0.1 mD (Fig. 18) for the dual-porosity signature to be clearly visible: that is, it is likely to occur more frequently in tight or unconventional reservoirs if there is no fracture damage. Secondly, the dual-porosity signature occurs at an early time during our simulations and, hence, may not always be captured in the field data. Figure 19a and b shows that even if the matrix block size increases from 20 m (base case) to 160 m, the dual-porosity V-shape is only visible within the first second of the well test. Larger matrix blocks (and increased fracture lengths) delay the onset of the dual-porosity signature relative to the base case because the fracture volume is increased and it takes slightly longer to deplete the fractures before the matrix recharge starts.

When applying the same changes in matrix permeability and matrix volume to the connected outcrop-based fracture patterns, (Fig. 9, lower inset) and simulating a well intersecting fractures, the same pressure response in Figures 18a and 19a is apparent in Figure 20a and b, respectively. Here, we rescaled the entire model dimensions and adjusted the fracture properties to ensure that the

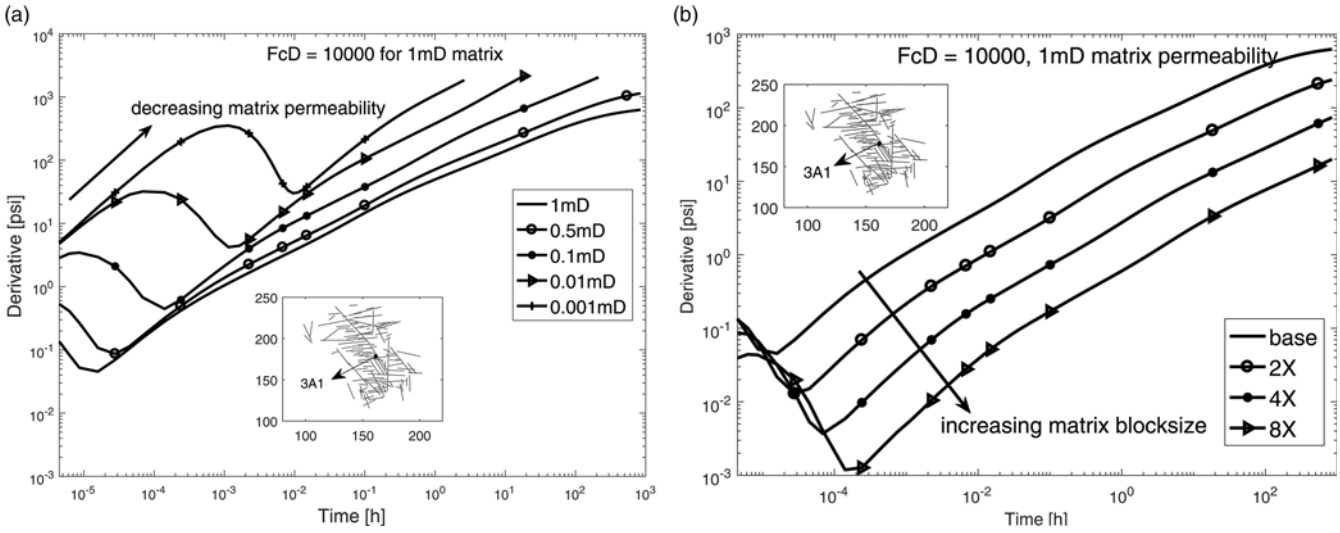

Fig. 20. Simulated pressure derivative of well-intersecting fractures in an outcrop fracture pattern with (**a**) decreasing matrix permeability ranging from 1 to 0.001 mD and (**b**) increasing matrix block size up to a factor of 8.

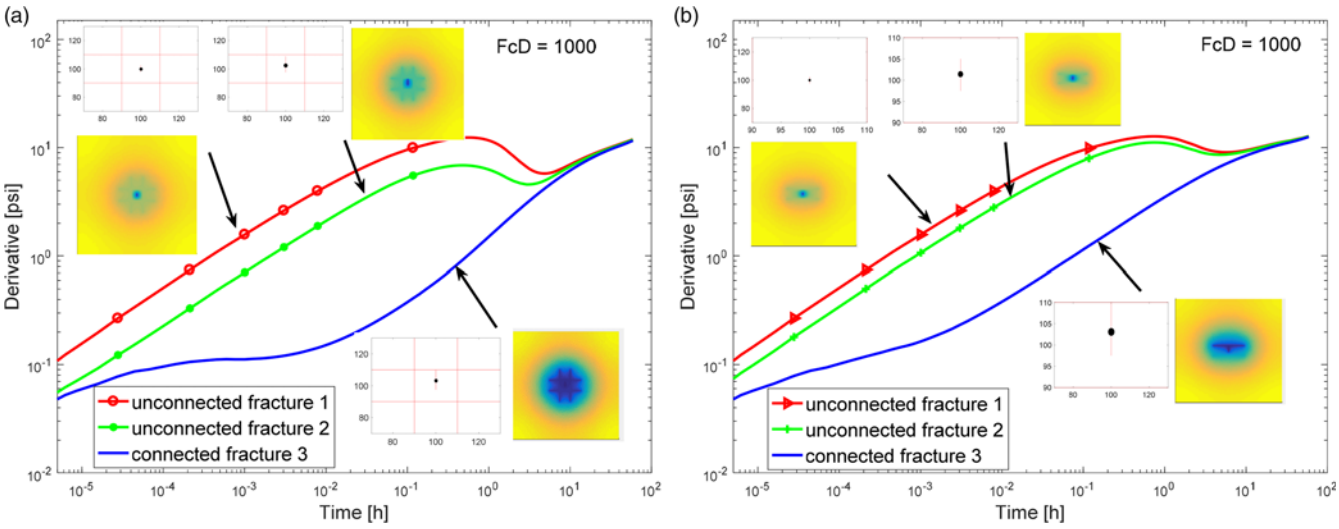

Fig. 21. Idealized models showing fracture geometry, simulated isobars around the well and pressure derivatives of smaller (un)connected fractures close to large fractures for a connected fracture network (**a**) and a disconnected fracture network (**b**).

fracture aperture remains unchanged: that is, the increase in fracture volume is only due to the increased fracture length, not to the fracture width.

Effect of fracture-network connectivity and size

We present another example where the dual-porosity signature can be observed for unrestricted interporosity flow even if the matrix permeability is high. This scenario occurs if the well intersects a fracture but this fracture belongs to a small fracture network or is an unconnected fracture that is located in, but not connected to, larger fracture(s). In these cases, fluids are first produced from the smaller fracture (network), then from the rock matrix and then from the larger network. This implies that the multiscale nature that is common to many fracture networks (e.g. Odling 1997) can be critical to the presence of the dual-porosity signature. To investigate this phenomenon quantitatively, we run a number of test simulations for both connected (Fig. 21a, insets) and disconnected fracture (Fig. 21b, insets) networks, and placed the well into an isolated fracture that is located close to, but not connected to, the larger fracture system. The fracture geometries differ from those shown previously in that they are even further idealized networks. Figure 21a and b shows the resulting pressure transients for the connected and disconnected networks, respectively. In each case, we observed that where the smaller fracture is not connected to the nearby large fracture(s), the first flow regime is either bilinear or linear flow, depending on the fracture conductivity. In the examples presented in these two figures with $F_{cD} = 1000$, the initial flow regime shows linear flow. Where the fracture is not surrounded by any other fracture, this initial flow regime changes to pseudo-radial flow, as illustrated in the single fracture case above (Fig. 7). However, where our simulation models contain other fractures surrounding the smaller ones that intersect the well, the resulting flow behaviour is significantly different after the initial flow period (Fig. 21a and b). Here, after the smaller fractures are depleted, the larger fractures begin to deplete just as the transient response from the small intersected fracture tends towards pseudo-radial flow with the surrounding matrix flow. This second depletion of the larger, nearby fractures yields the dual-porosity V-shape observed here. After this dual-porosity behaviour ceases, the entire system then stabilizes. However, the moment the smaller fracture is connected to any of the surrounding large fractures, the dual-behaviour signature

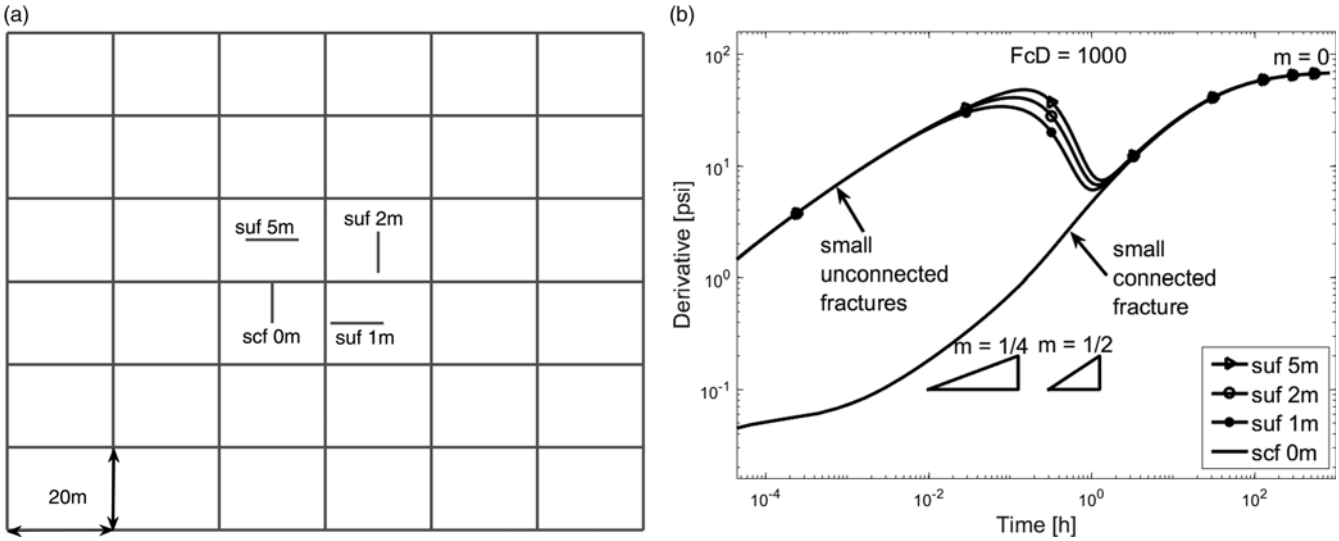

Fig. 22. A well intersecting smaller (un)connected fractures in an idealized connected fracture network. Fracture geometry with a 5, 2 and 1 m separation distance between smaller fractures and the large fractures (**a**) and simulated pressure derivatives of the configurations shown (**b**).

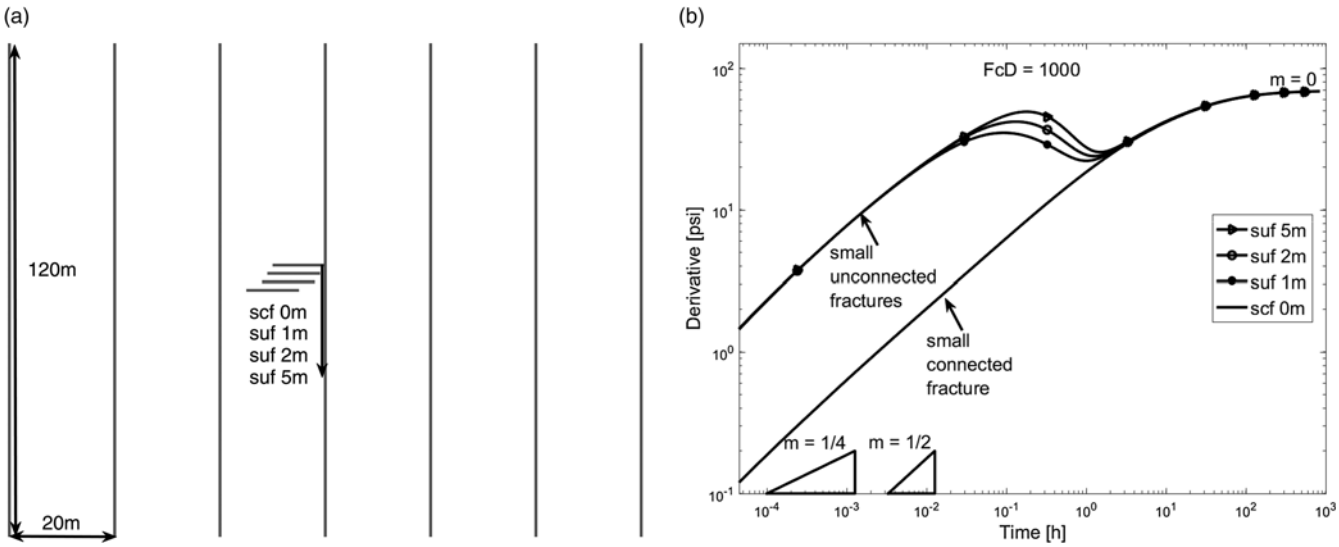

Fig. 23. A well intersecting smaller (un)connected fractures in an idealized disconnected fracture network. Fracture geometry with a 5, 2 and 1 m separation distance between smaller fractures and the large fractures (**a**) and simulated pressure derivatives of the configurations shown (**b**).

disappears because the entire fracture network responds as one single network.

The dependence of the dual-porosity signature on wells located in small-scale fractures that are disconnected from the larger-sale fractures is independent of the fracture geometries. Figures 22b and 23b show the pressure transients for the idealized connected fracture networks (Fig. 22a; see the further description in Table 2, Model 8) and disconnected fracture networks (Fig. 23a; see the further description in Table 2, Model 9). In the disconnected fracture network, smaller disconnected fractures have been added but are kept separated from the closest large fracture by distances of 5, 2 and 1 m, respectively. Importantly, the orientation of the minor fractures does not impact on the presence or absence of the dual-porosity signature; only the distance of the separation between the fractures is important. As noted above, the fracture half-length can be estimated from the linear flow regime. Here, we estimate the fracture half-length of the small fracture from the early linear flow regime. When the small fracture is connected to the nearby large fractures, the flow behaviour is different. Figure 22b shows that the small connected fracture profile is an S-shape, consistent with our results for a connected fracture network presented in Figure 11a. In the disconnected fracture network (Fig. 23b), the minor connected fracture results in a linear flow regime which then transitions to pseudo-radial flow, as already observed in the findings shown in Figure 12a. The half-length estimated from the linear flow regime in the disconnected fracture network corresponds to that of the combined lengths of the small and large fractures. This is in contrast to the situation where the small fracture is isolated and only the length of the small fracture can be estimated. Results presented in Figures 21–23 confirm that a fractured reservoir with an unrestricted interporosity flow generates a dual-porosity signature if the well is intersecting a smaller fracture located close to a large fracture or fracture network.

However, not all small fractures that are disconnected from the larger fractures cause a clear dual-porosity behaviour (i.e. the V-shape profile of Warren & Root 1963). To quantify when the small, disconnected fractures cause a dual-porosity signature, we established a simple relationship, the effective length ratio (ELR), between the

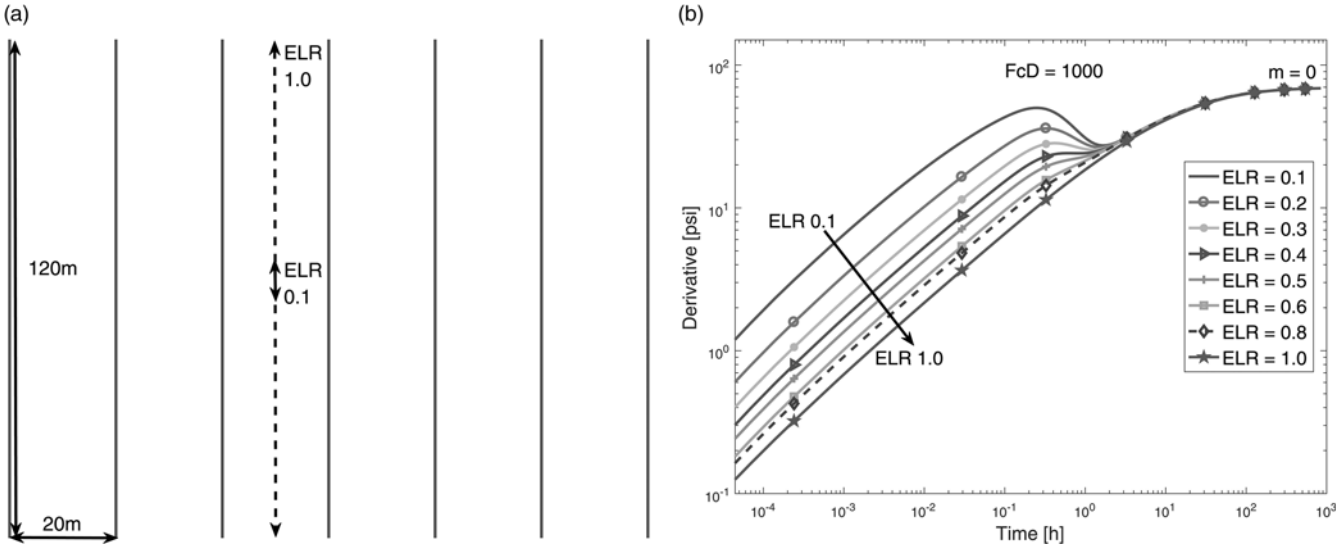

Fig. 24. A well intersecting smaller unconnected fractures in an idealized disconnected fracture network. Fracture geometry with an increasing length (ELR of 0.1–1) of a smaller fracture located close to large fractures (units in metres) (**a**) and simulated pressure derivatives of the configurations shown (**b**). ELR is the effective length ratio defined in equation (8).

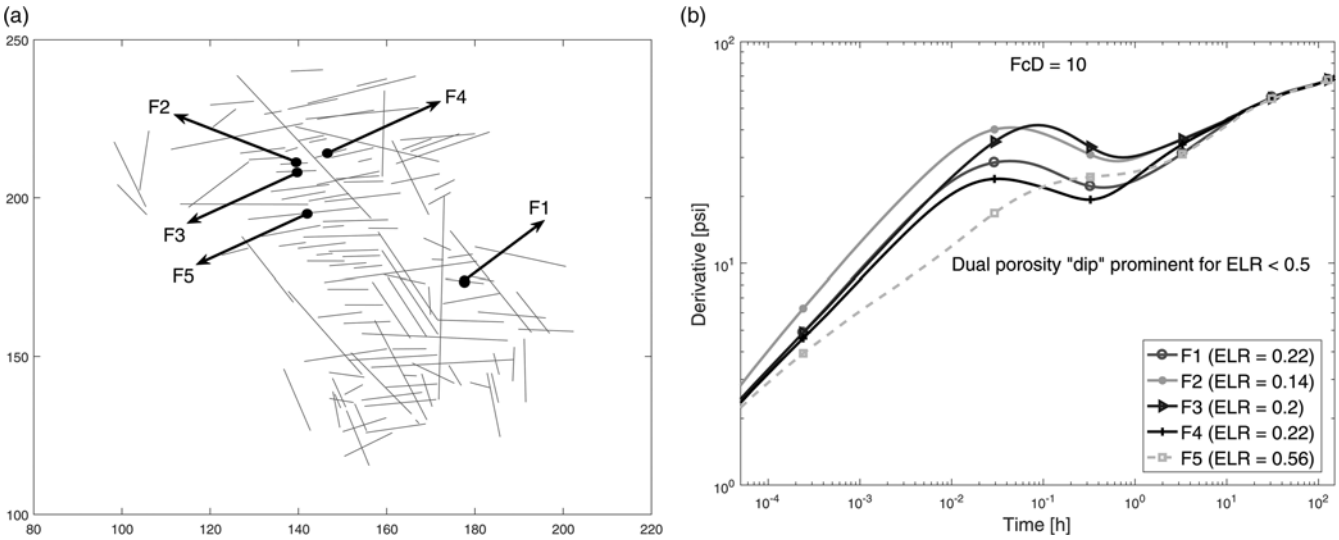

Fig. 25. A well intersecting smaller unconnected fractures located in the Jandaira Formation (Fig. 9, lower inset). Fracture geometry with variable lengths of fractures and separation distances between smaller fractures and the large fractures (**a**) and simulated pressure derivatives of the configurations shown (**b**).

lengths of the small and large fracture(s). We define ELR as:

$$\text{ELR} = \frac{l_{\text{suf}}}{L_{\text{lf}}} \tag{8}$$

where l_{suf} and L_{lf} denote the length of the small unconnected fracture and the length of the nearby large fracture, respectively.

Using this relationship, we ran simulations on the idealized disconnected fracture networks, adding fractures with ELRs ranging from 0.1 to 1.0 (Fig. 24a; see the further description in Table 2, Model 10). The resulting pressure transients (Fig. 24b) show that the dual-porosity signature is more prominent when the length of the smaller fracture is small compared to the nearby larger fracture. As the value of ELR increases, the dual-porosity signature diminishes. Once ELR exceeds 0.5, the dual-porosity signature is absent. Furthermore, it can be observed from Figure 24(b) that the symmetry of the limbs of the dual-porosity 'dip' is also a function of the ELR. Small values of ELR tend to yield a 'V-shape' curve with first limbs (upper-left to bottom-right direction) that are more symmetrical to the second limbs (bottom-left to upper-right direction), while large ELR values produce first limbs that are asymmetrical to the other limb. Flow regimes identified prior to the emergence of this first limb depend on the properties of the smaller fracture intersected by the well. The second limb of this shape relates to the fracture conductivity and nature of the fracture-network connectivity.

The impact of ELR on the dual-porosity behaviour is also apparent in the outcrop-based fracture patterns (shown in Fig. 9, lower inset). We identified unconnected smaller fractures with different lengths (Fig. 25a), calculated the corresponding ELR and simulated the pressure transients (Fig. 25b) for cases where the well intersects these smaller fractures. The results show a clear dual-porosity signature for all cases, except for case F5 where ELR = 0.56 (i.e. above the cut-off value of 0.5).

Conclusions

We applied a geoengineering workflow with the discrete fracture matrix modelling (DFM) technique and unstructured-grid reservoir simulator to generate synthetic pressure transient responses for idealized fractures and realistic fracture networks. We demonstrated when dual-porosity models are valid and systematically present alternative interpretations to reservoir features that characterize this behaviour in naturally fractured reservoirs. Furthermore, we quantified when and why the assumptions break down when interpreting well-test data from naturally fractured reservoirs.

Based on the numerical simulations and the results presented, we arrived at the following conclusions:

- For a well intersecting a fracture, the dual-porosity 'dip' of the Warren & Root (1963) well-testing signature is observed in Type II and III of Nelson's (2001) classification due to the following situations:
  - the effect of the fracture skin, similar to that in Cinco-Ley & Samaniego (1977);
  - the matrix permeability is very tight (<1 mD), similar to unconventional reservoirs (e.g. tight gas sands);
  - the well intersects a small unconnected fracture located near a single large fracture or a large fracture network.
- Reservoirs can be fractured even if the dual-porosity 'V-shape' in the well-test data is absent.

Natural fractures have a significant effect on hydrocarbon recovery and reservoir productivity. Therefore, it is critical to identify fractures and assess the flow behaviour early on during a development to improve reservoir performance and optimize recovery. A reservoir characterization that relies on the appearance of a dual-porosity V-shape on pressure derivatives reduces the chance of identifying and properly interpreting fractures from well-test data. If not properly characterized (or missed), fractures could cause production issues and result in a detrimental effect on hydrocarbon recovery, including early water and gas breakthrough. Our results show a range in flow behaviour from a pressure transient analysis that could indicate the presence of fractures in a reservoir where the classic dual-porosity V-shape is absent.

However, where the conventional dual-porosity signature is recognizable, we provided insight into the key geological features (including fracture skin, matrix permeability, fracture-network connectivity and size) that characterize this response. Our findings on wells intersecting smaller fractures give insight into the occurrence of fracture-network sizes and their connectivity in a field. Identification and quantification of multiscale fractures is invaluable in assessing the role of different fracture sets during production. The influence of these fractures can be harnessed when planning IOR/EOR schemes to improve recovery.

We observed that the limbs of the dual-porosity 'dip' can provide further diagnosis about the fracture-network conductivity and connectivity. Generally, a shallow symmetrical 'dip' indicates low

fracture conductivities, and a steep 'dip' points to high fracture conductivities. For the high fracture conductivity cases, the second limb of the 'V-shape' can differentiate a connected fracture network (with ½ slope) from a disconnected fracture network (with ¼ slope). Where the dual-porosity 'dip' results from the well intersecting a small-unconnected fracture located near a large fracture or fracture network, the symmetry of the first limb to the second is a function of the small fracture.

Acknowledgements We thank CMG Ltd for access to IMEX, Weatherford for access to Pansystem, and SINTEF for access to MRST and their support with MRST. We also thank Petrobras and the Brazilian Agency of Petroleum and Biofuels (Agência Nacional do Petróleo, ANP) for field work support.

Funding Authors are grateful to the Petroleum Technology Development Fund (NG) for funding David Egya's PhD, to Energi Simulation (CA) for supporting Sebastian Geiger's Chair for Carbonate Reservoir Simulation and BG Group International for Patrick Corbett's Chair for Carbonate Petroleum Geoengineering. We further thank Molengraaff funds of the Delft University of Technology (NL) for supporting Kevin Bisdom's research and Petrobras (BR) for sponsoring Francisco Bezerra's fieldwork.

References

Abbaszadeh, M. & Cinco-Ley, H. 1995. Pressure-transient behavior in a reservoir with a finite-conductivity fault. *SPE Formation Evaluation*, **10**, 26–32, https://doi.org/10.2118/24704-PA

Agada, S., Chen, F., Geiger, S., Toigulova, G., Agar, S., Shekhar, R. & Immenhauser, A. 2014. Numerical simulation of fluid-flow processes in a 3D high-resolution carbonate reservoir analogue. *Petroleum Geoscience*, **20**, 125–142, https://doi.org/10.1144/petgeo2012-096

Agar, S.M., Geiger, S. & Matthäi, S.K. 2010. The impact of hierarchical fracture networks on flow partitioning in carbonate reservoirs: examples based on a Jurassic carbonate ramp analog from the High Atlas, Morocco. *SPE Annual Technical Conference and Exhibition*, **2**, 1–19, https://doi.org/10.2118/135135-MS

Ahmadov, R., Aydin, A., Karimi-Fard, M. & Durlofsky, L.J. 2007. Permeability upscaling of fault zones in the Aztec Sandstone, Valley of Fire State Park, Nevada, with a focus on slip surfaces and slip bands. *Hydrogeology Journal*, **15**, 1239–1250, https://doi.org/10.1007/s10040-007-0180-2

Aljuboori, F., Bisdom, K., Corbett, P.W.M., Bertotti, G. & Geiger, S. 2015. Using outcrop data for geological well test modelling in fractured reservoirs. Paper presented at the 77th EAGE Conference & Exhibition, 1–4 June 2015, Madrid, Spain.

Bahrainian, S.S., Dezfuli, A.D. & Noghrehabadi, A. 2015. Unstructured grid generation in porous domains for flow simulations with discrete-fracture network model. *Transport in Porous Media*, **109**, 693–709, https://doi.org/10.1007/s11242-015-0544-3

Barenblatt, G., Zheltov, I. & Kochina, I. 1960. Basic concepts in the theory of seepage of homogeneous liquids in fissured rocks [strata]. *Journal of Applied Mathematics and Mechanics*, **24**, 1286–1303, https://doi.org/10.1016/0021-8928(60)90107-6

Belayneh, M., Geiger, S. & Matthäi, S.K. 2006. Numerical simulation of water injection into layered fractured carbonate reservoir analogs. *AAPG Bulletin*, **90**, 1473–1493, https://doi.org/10.1306/05090605153

Belayneh, M., Matthai, S. & Cosgrove, J. 2007. The implications of fracture swarms in the Chalk of SE England on the tectonic history of the basin and their impact on fluid flow in high-porosity, low-permeability rocks. *In*: Ries, A.C., Butler, R.W.H. & Graham, R.H. (eds) *Deformation of the Continental Crust: The Legacy of Mike Coward*. Geological Society, London, Special Publications, **272**, 499–517, https://doi.org/10.1144/GSL.SP.2007.272.01.25

Belayneh, M.W., Matthai, S.K., Blunt, M.J. & Rogers, S.F. 2009. Comparison of deterministic with stochastic fracture models in water-flooding numerical simulations. *AAPG Bulletin*, **93**, 1633–1648, https://doi.org/10.1306/07220909031

Beliveau, D., Payne, D. & Mundry, M. 1993. Waterflood and CO_2 flood of the fractured Midale Field (includes associated paper 22947). *Journal of Petroleum Technology*, **45**, 881–887, https://doi.org/10.2118/22946-PA

Bertotti, G., Bisdom, K., van Eijk, M., Hameka, F., Vis, A., Bezerra, H. & Reijmer, J. 2014. Fractures and fracture networks in carbonate reservoirs: a geological perspective. Paper presented at the AAPG International Conference & Exhibition, 14–17 September 2014. Istanbul, Turkey.

Bertotti, G., de Graaf, S. *et al.* 2017. Fracturing and fluid-flow during post-rift subsidence in carbonate of the Jandaíra Formation, Potiguar Basin, NE Brazil. *Basin Research*, **29**, 836–853, https://doi.org/10.1111/bre.12246

Berumen, S., Tiab, D. & Rodriguez, F. 2000. Constant rate solutions for a fractured well with an asymmetric fracture. *Journal of Petroleum Science and Engineering*, **25**, 49–58, https://doi.org/10.1016/S0920-4105(99)00053-4

Bisdom, K., Bertotti, G. & Nick, H.M. 2016. The impact of different aperture distribution models and critical stress criteria on equivalent permeability in fractured rocks. *Journal of Geophysical Research: Solid Earth*, **119**, 8132–8153, https://doi.org/10.1002/2015JB012657

Bisdom, K., Bertotti, G. & Bezerra, F.H. 2017*a*. Inter-well scale natural fracture geometry and permeability variations in low-deformation carbonate rocks. *Journal of Structural Geology*, **97**, 23–36, https://doi.org/10.1016/j.jsg.2017.02.011

Bisdom, K., Nick, H.M. & Bertotti, G. 2017*b*. An integrated workflow for stress and flow modelling using outcrop-derived discrete fracture networks. *Computers & Geosciences*, **103**, 21–35, https://doi.org/10.1016/j.cageo.2017.02.019

Bogdanov, I.I., Mourzenko, V.V., Thovert, J.-F.& Adler, P.M. 2003. Pressure drawdown well tests in fractured porous media. *Water Resources Research*, **39**, 1021, https://doi.org/10.1029/2000WR000080

Boulton, N.S. & Streltsova, T.D. 1977. Unsteady flow to a pumped well in a fissured water-bearing formation. *Journal of Hydrology*, **35**, 257–270.

Bourbiaux, B. 2010. Fractured reservoir simulation: a challenging and rewarding issue. *Oil & Gas Science and Technology – Revue de l'Institut Français du Pétrole*, **65**, 227–238, https://doi.org/10.2516/ogst/2009063

Bourdet, D. 2002. *Well Test Analysis: The Use of Advanced Interpretation Models Handbook of Petroleum Exploration and Production. Volume 3*. Elsevier, Amsterdam.

Bourdet, D. & Gringarten, A.C. 1980. Determination of fissure volume and block size in fractured reservoirs by type-curve analysis. Paper presented at the SPE Annual Technical Conference and Exhibition, 21–24 September 1980, Dallas, Texas, USA, https://doi.org/10.2118/9293-MS

Bourdet, D., Ayoub, J. & Kniazeff, V. 1983*a*. Interpreting well tests in fractured reservoirs. *World Oil*, **197**, 77–87.

Bourdet, D., Whittle, T.M., Douglas, A.A. & Pirard, Y.M. 1983*b*. A new set of type curves simplifies well test analysis. *World Oil*, **196**, 95–106, https://doi.org/10.2118/16812-PA

Bourdet, D., Ayoub, J.A. & Pirard, Y.M. 1989. Use of pressure derivative in well test interpretation. *SPE Formation Evaluation*, **4**, 293–302, https://doi.org/10.2118/12777-PA

Branets, L.V., Ghai, S.S., Lyons, S.L.L. & Wu, X.-H. 2009. Challenges and technologies in reservoir modeling. *Communications in Computational Physics*, **6**, 1–23, https://doi.org/10.4208/cicp.2009.v6.p1

Chen, Z.-X. 1989. Transient flow of slightly compressible fluids through double porosity, double-permeability systems–a state-of-the-art review. *Transport in Porous Media*, **4**, 147–184.

Cinco-Ley, H. 1996. Well-testing analysis for naturally fractured reservoirs. *Journal of Petroleum Technology*, **48**, 51–54.

Cinco-Ley, H. & Samaniego, V.F. 1977. Effect of wellbore storage and damage on the transient pressure behavior of vertically fractured wells. Paper presented at the SPE Annual Fall Technical Conference and Exhibition, 9–12 October 1977, Denver, Colorado, USA.

Cinco-Ley, H. & Samaniego, V.F. 1981. Transient pressure analysis for fractured wells. *Journal of Petroleum Technology*, **33**, 1749–1766, https://doi.org/10.2118/7490-PA

Cinco-Ley, H. & Samaniego, V.F. 1982. Pressure transient analysis for naturally fractured reservoirs. Paper presented at the SPE Annual Technical Conference and Exhibition, 26–29 September 1982, New Orleans, Louisiana, USA, https://doi.org/10.2118/11026-MS

Cinco-Ley, H., Samaniego, V.F. & Dominguez, A.N. 1976. Unsteady-state flow behavior for a well near a natural fracture. Paper presented at the SPE Annual Fall Technical Conference and Exhibition, 3–6 October 1976, New Orleans, Louisiana, USA.

Cinco-Ley, H., Samaniego, V.F. & Kucuk, F. 1985. The pressure transient behavior for naturally fractured reservoirs with multiple block size. Paper presented at the SPE Annual Technical Conference and Exhibition, 22–25 September 1985, Las Vagas, Nevada, USA.

Corbett, P.W.M., Geiger, S., Borges, L., Garayev, M. & Valdez, C. 2012. The third porosity system: understanding the role of hidden pore systems in well-test interpretation in carbonates. *Petroleum Geoscience*, **18**, 73–81, https://doi.org/10.1144/1354-079311-010

de Graaf, S., Reijmer, J.J.G., Bertotti, G.V., Bezerra, F.H.R., Cazarin, C.L., Bisdom, K. & Vonhof, H.B. 2017. Fracturing and calcite cementation controlling fluid flow in the shallow-water carbonates of the Jandaíra Formation, Brazil. *Marine and Petroleum Geology*, **80**, 382–393, https://doi.org/10.1016/j.marpetgeo.2016.12.014

de Swaan O.A. 1976. Analytic solutions for determining naturally fractured reservoir properties by well testing. *Society of Petroleum Engineers Journal*, **16**, 117–122, https://doi.org/10.2118/5346-PA

Earlougher, R.C.J. 1977. *Advances in Well Test Analysis*. Society of Petroleum Engineers of AIME, Dallas, Monograph,**264**.

Edery, Y., Porta, G.M., Guadagnini, A., Scher, H. & Berkowitz, B. 2016. Characterization of bimolecular reactive transport in heterogeneous porous media. *Transport in Porous Media*, **115**, 291–310, https://doi.org/10.1007/s11242-016-0684-0

Egya, D., Geiger, S., Corbett, P., March, R., Bisdom, K., Bertotti, G. & Bezerra, H. 2016. Assessing the validity and limitations of dual-porosity models using geological well testing for fractured formations. Paper presented at the 78th EAGE Conference & Exhibition 2016, 30 May–2 June 2016, Vienna, Austria.

Egya, D., Geiger, S., Corbett, P. & March, R. 2017. The effect of fracture skin, network connectivity, and network size on well-test responses in naturally

fractured reservoirs. Paper presented at the 79th EAGE Conference & Exhibition, 12–15 June 2017, Paris, France.
Fernø, M. 2012. Enhanced oil recovery in fractured reservoirs. *In:* Romero-Zerón, L. (ed.) *Introduction to Enhanced Oil Recovery (EOR) Processes and Bioremediation of Oil-Contaminated Sites*, 89–110. InTech, Rijeka, Croatia, 89–110, retrieved from http://cdn.intechopen.com/pdfs/37039.pdf
Firoozabadi, A. 2000. Recovery mechanisms in fractured reservoirs and field performance. *Journal of Canadian Petroleum Technology*, **39**, 13–17, https://doi.org/10.2118/00-11-DAS
Geiger, S. & Emmanuel, S. 2010. Non-Fourier thermal transport in fractured geological media. *Water Resources Research*, **46**, 1–13, https://doi.org/10.1029/2009WR008671
Geiger, S. & Matthäi, S. 2014. What can we learn from high-resolution numerical simulations of single- and multi-phase fluid flow in fractured outcrop analogues? *In*: Spence, G.H., Redfern, J., Aguilera, R., Bevan, T.G., Cosgrove, J.W., Couples, G.D. & Daniel, J.-M. (eds) *Advances in the Study of Fractured Reservoirs*. Geological Society, London, Special Publications, **374**, 125–144, https://doi.org/10.1144/SP374.8
Geiger, S., Matthäi, S., Niessner, J. & Helmig, R. 2009. Black-oil simulations for three-component, three-phase flow in fractured porous media. *Society o Petroleum Engineers Journal*, **14**, 338–354, https://doi.org/10.2118/107485-PA
Geiger, S., Dentz, M. & Neuweiler, I. 2013. A novel multi-rate dual-porosity model for improved simulation of fractured and multiporosity reservoirs. *Society of Petroleum Engineers Journal*, **18**, 670–684, https://doi.org/10.2118/148130-MS
Gilman, J.R. & Kazemi, H. 1983. Improvements in simulation of naturally fractured reservoirs. *Society of Petroleum Engineers Journal*, **23**, 695–707, https://doi.org/10.2118/10511-PA
Gringarten, A.C. 1984. Interpretation of tests in fissured and multilayered reservoirs with double porosity behavior: theory and practice. *Journal of Petroleum Technology*, **36**, 549–564.
Gringarten, A.C. 1987. How to recognize 'double-porosity' systems from well tests. *Journal of Petroleum Technology*, **39**, 631–633, https://doi.org/10.2118/16437-PA
Gringarten, A.C., Ramey, H.J. & Raghavan, R. 1974. Unsteady-state pressure distributions created by a well with a single infinite-conductivity vertical fracture. *Society of Petroleum Engineers Journal*, **14**, 347–360.
Gringarten, A.C., Ramey, H.J., Jr & Raghavan, R. 1975. Applied pressure analysis for fractured wells. *Journal of Petroleum Technology*, **27**, 887–892, https://doi.org/10.2118/5496-PA
Hardebol, N.J., Maier, C., Nick, H., Geiger, S., Bertotti, G. & Boro, H. 2015. Multiscale fracture network characterisation and impact on flow : A case study on the Latemar carbonate platform. *Journal of Geophysical Research: Solid Earth*, **120**, 8197–8222, https://doi.org/10.1002/2015JB011879
Howell, J.A., Martinius, A.W. & Good, T.R. 2014. The application of outcrop analogues in geological modelling: a review, present status and future outlook. *In:* Martinius, A.W., Howell, J.A. & Good, T.R. (eds) *Sediment-Body Geometry and Heterogeneity: Analogue Studies for Modelling the Subsurface*. Geological Society, London, Special Publications, **387**, 1–25, https://doi.org/10.1144/SP387.12
Hyman, J.D., Gable, C.W., Painter, S.L. & Makedonska, N. 2014. Conforming Delaunay triangulation of stochastically generated three dimensional discrete fracture networks: a feature rejection algorithm for meshing strategy. *SIAM Journal on Scientific Computing*, **36**, 1871–1894.
KAPPA. 2012. KAPPA *Dynamic Data Analysis (DDA) - v4.12.03*.
Karimi-Fard, M., Durlofsky, L.J. & Aziz, K. 2004. An efficient discrete-fracture model applicable for general-purpose reservoir simulators. *Society of Petroleum Engineers Journal*, **9**, 227–236, https://doi.org/10.2118/88812-PA
Kazemi, H. 1969. Pressure transient analysis of naturally fractured reservoirs with uniform fracture distribution. *Society of Petroleum Engineers Journal*, **9**, 451–462, https://doi.org/10.2118/2156-A
Kazemi, H., Seth, M.S. & Thomas, G.W. 1969. The interpretation of interference tests in naturally fractured reservoirs with uniform fracture distribution. *Society of Petroleum Engineers Journal*, **9**, 463–472, https://doi.org/10.2118/2156-PA
Kim, J.-G. & Deo, M.D. 2000. Finite element, discrete-fracture model for multiphase flow in porous media. *AIChE Journal*, **46**, 1120–1130, https://doi.org/10.1002/aic.690460604
Kuchuk, F. & Biryukov, D. 2014. Pressure-transient behavior of continuously and discretely fractured reservoirs. *SPE Reservoir Evaluation & Engineering*, **17**, 82–97, https://doi.org/10.2118/158096-PA
Kuchuk, F. & Biryukov, D. 2015. Pressure-transient tests and flow regimes in fractured reservoirs. *SPE Reservoir Evaluation and Engineering*, **18**, 187–204.
Kuchuk, F., Biryukov, D. & Fitzpatrick, T. 2015. Fractured-reservoir modeling and interpretation. *Society of Petroleum Engineers Journal*, **20**, 983–1004.
Lemonnier, P. & Bourbiaux, B. 2010*a*. Simulation of naturally fractured reservoirs. state of the art. Part 1 – physical mechanisms and simulator formulation. *Oil & Gas Science and Technology – Revue de l'Institut Français du Pétrole*, **65**, 239–262, https://doi.org/10.2516/ogst/2009066
Lemonnier, P. & Bourbiaux, B. 2010*b*. Simulation of naturally fractured reservoirs. state of the art. Part 2 – matrix-fracture transfers and typical features of numerical studies. *Oil & Gas Science and Technology – Revue de l'Institut Français du Pétrole*, **65**, 263–286, https://doi.org/10.2516/ogst/2009067
Lie, K.-A., Krogstad, I.S., Natvig, J.R., Nilsen, H.M. & Skaflestad, B. 2012. Open-source MATLAB implementation of consistent discretisations on complex grids. *Computational Geosciences*, **16**, 297–322.
Mallison, B.T., Hui, M.H. & Narr, W. 2010. Practical gridding algorithms for discrete fracture modeling workflows. Paper presented at the ECMOR XII, 12th European Conference on the Mathematics of Oil Recovery, 6–9 September 2010, Oxford, UK, https://doi.org/A032
Matthäi, S.K. & Belayneh, M. 2004. Fluid flow partitioning between fractures and a permeable rock matrix. *Geophysical Research Letters*, **31**, 1–5, https://doi.org/10.1029/2003GL019027
Matthäi, S.K. & Roberts, S.G. 1996. The influence of fault permeability on single-phase fluid flow near fault-sand intersections: Results from steady-state high-resolution models of pressure-driven fluid flow. *AAPG Bulletin*, **80**, 1763–1779, https://doi.org/10.1306/64EDA15E-1724-11D7-8645000102C1865D
Mavor, M.J. & Cinco-Ley, H. 1979. Transient pressure behavior of naturally fractured reservoirs. Paper presented at the SPE California Regional Meeting, 18–20 April 1979, Ventura, California, USA.
Moench, A.F. 1984. Double-porosity models for a fissured groundwater reservoir with fracture skin. *Water Resources Research*, **20**, 831–846.
Morton, K.L., Nogueira, P. de B., Booth, R.J.S. & Kuchuk, F.J. 2012. Integrated interpretation for pressure transient tests in discretely fractured reservoirs. Paper presented at the EAGE Conference & Exhibition incorporating SPE EUROPEC 2012, 4–7 June 2012, Copenhagen, Denmark.
Morton, K.L., Booth, R.J.S., Chugunov, N., Biryukov, D., Fitzpatrick, A.F. & Kuchuk, F.J. 2013. Global sensitivity analysis for natural fracture geological modeling parameters from pressure transient tests. Paper presented at the EAGE Annual Conference & Exhibition incorporating SPE EUROPEC 2013, 10–13 June 2013, London, UK.
Morton, K.L., Kuchuk, F.J. & Fitzpatrick, A.J. 2015. Active and interference well pressure transient data interpretation in naturally fractured reservoirs. Paper presented at the 77th EAGE Conference & Exhibition, 1–4 June 2015, Madrid, Spain.
Møyner, O. & Lie, K.-A. 2016. A multiscale restriction-smoothed basis method for high contrast porous media represented on unstructured grids. *Journal of Computational Physics*, **304**, 46–71, https://doi.org/10.1016/j.jcp.2015.10.010
Najurieta, H.L. 1980. A theory for pressure transient analysis in naturally fractured reservoirs. *Journal of Petroleum Technology*, **32**, 1–241.
Narr, W., Schechter, D.W. & Thompson, L.B. 2006. *Naturally Fractured Reservoir Characterization*. Society of Petroleum Engineers, Richardson, Texas, USA.
Nelson, R.A. 2001. *Geologic Analysis of Naturally Fractured Reservoirs*. Gulf Professional Publishing, Houston, Texas, USA.
Odeh, A.S. 1965. Unsteady-state behavior of naturally fractured reservoirs. *Society of Petroleum Engineers Journal*, **5**, 60–66, https://doi.org/10.2118/966-PA
Odling, N.E. 1997. Scaling and connectivity of joint systems in sandstones from western Norway. *Journal of Structural Geology*, **19**, 1257–1271, https://doi.org/10.1016/S0191-8141(97)00041-2
Olorode, O.M., Freeman, C.M., Moridis, G.J. & Blasingame, T.A. 2013. High-resolution numerical modeling of complex and irregular fracture patterns in shale-gas reservoirs and tight gas reservoirs. *SPE Reservoir Evaluation & Engineering*, **16**, 443–455.
Ramsey, J.M. & Chester, F.M. 2004. Hybrid fracture and the transition from extension fracture to shear fracture. *Nature*, **428**, 63–66, https://doi.org/10.1038/nature02333
Seers, T.D. & Hodgetts, D. 2013. Comparison of digital outcrop and conventional data collection approaches for the characterization of naturally fractured reservoir analogues. *In*: Spence, G.H., Redfern, J., Aguilera, R., Bevan, T.G., Cosgrove, J.W., Couples, G.D., & Daniel, J.-M. (eds) *Advances in the Study of Fractured Reservoirs*. Geological Society, London, Special Publications, **374**, 51–77, https://doi.org/10.1144/SP374.13
Serra, K., Reynolds, A. & Raghavan, R. 1983. New pressure transient analysis methods for naturally fractured reservoirs. *Journal of Petroleum Technology*, **35**, 2271–2283, https://doi.org/10.2118/10780-PA
Shewchuck, J.R. 2002. Delaunay refinement algorithms for triangular mesh generation. *Applied Computational Geometry*, **22**, 21–74, https://doi.org/10.1016/S0925-7721(01)00047-5
Spence, G.H., Couples, G.D., Bevan, T.G., Aguilera, R., Cosgrove, J.W., Daniel, J.-M. & Redfern, J. 2014. Advances in the study of naturally fractured hydrocarbon reservoirs: a broad integrated interdisciplinary applied topic. *In:* Spence, G.H., Couples, G.D., Bevan, T.G., Aguilera, R., Cosgrove, J.W., Daniel, J.-M. & Redfern, J. (eds) *Advances in the Study of Fractured Reservoirs*. Geological Society, London, Special Publications, **374**, 1–22, https://doi.org/10.1144/SP374.19
Streltsova, T.D. 1976. Hydrodynamics of groundwater flow in a fractured formation. *Water Resources Research*, **12**, 405–414, https://doi.org/10.1029/WR012i003p00405
Streltsova, T.D. 1983. Well pressure behavior of a naturally fractured reservoir. *Society of Petroleum Engineers Journal*, **23**, 769–780.
Sun, J. & Schechter, D. 2015. Optimization-based unstructured meshing algorithms for simulation of hydraulically and naturally fractured reservoirs with variable distribution of fracture aperture, spacing, length and strike. *SPE Reservoir Evaluation & Engineering*, **18**, 463–480.

Sun, J., Schechter, D., Texas, A. & Huang, C. 2015. Sensitivity analysis of unstructured meshing parameters on production forecast of hydraulically fractured horizontal wells. Paper presented at the SPE Abu Dhabi International Petroleum Exhibition and Conference, 9–12 November 2015, Abu Dhabi, UAE, https://doi.org/10.2118/177480-MS

Syihab, Z. 2009. *Simulation of discrete fracture network using flexible Voronoi gridding*. Doctoral dissertation, Texas A&M University, College Station, Texas, USA.

Valdes-Perez, A.R., Pulido, H., Cinco-Ley, H. & Galicia-muñoz, G. 2011. A new bilinear flow model for naturally fractured reservoirs with transient interporosity transfer. Proceedings of the Thirty-Sixth Workshop on Geothermal Reservoir Engineering Stanford University, Stanford, California, January 31–February 2, 2011.

Wanjing, L. & Changfu, T. 2014. Pressure-transient analysis of multiwing fractures connected to a vertical wellbore. *Society of Petroleum Engineers Journal*, **20**, 360–367.

Warren, J.E. & Root, P.J. 1963. The behavior of naturally fractured reservoirs. *Society of Petroleum Engineers Journal*, **3**, 245–255.

Wei, L., Hadwin, J., Chaput, E., Rawnsley, K. & Swaby, P. 1998. Discriminating fracture patterns in fractured reservoirs by pressure transient tests. Paper SPE 49233 presented at the SPE Annual Technical Conference and Exhibition, 27–30 September 1998, New Orleans, Louisiana, USA.

Wilson, C.E., Aydin, A. *et al.* 2011. From outcrop to flow simulation: Constructing discrete fracture models from a LIDAR survey. *AAPG Bulletin*, **95**, 1883–1906, https://doi.org/10.1306/03241108148

Wong, D.W., Harrington, A.G. & Cinco-Ley, H. 1986. Application of the pressure derivative function in the pressure transient testing of fractured wells. *SPE Formation Evaluation*, **1**, 470–480, https://doi.org/10.2118/13056-PA

Zheng, S.Y., Legrand, V.M. & Corbett, P.W.M. 2007. Geological model evaluation through well test simulation: a case study from the Wytch farm oilfield, southern England. *Journal of Petroleum Geology*, **30**, 41–58.

Zhou, F., Shi, A. & Wang, X. 2014. An efficient finite difference model for multiphase flow in fractured reservoirs. *Petroleum Exploration and Development*, **41**, 262–266, https://doi.org/10.1016/S1876-3804(14)60031-8